



## 12 **ABSTRACT**

13 Protein tyrosine phosphatases non-receptor type (PTPNs) have been studied extensively in the  
14 context of the adaptive immune system; however, their roles beyond immunoregulation are  
15 less well explored. Here we identify novel functions for the conserved *C. elegans* phosphatase  
16 PTPN-22, establishing its role in nematode molting, cell adhesion, and cytoskeletal regulation.  
17 Through a non-biased genetic screen, we found that loss of PTPN-22 phosphatase activity  
18 suppressed molting defects caused by loss-of-function mutations in the conserved NIMA-  
19 related kinases NEKL-2 (human NEK8/NEK9) and NEKL-3 (human NEK6/NEK7), which act at the  
20 interface of membrane trafficking and actin regulation. To better understand the functions of  
21 PTPN-22, we carried out proximity labeling studies to identify candidate interactors of PTPN-22  
22 during development. Through this approach we identified the CDC42 guanine-nucleotide  
23 exchange factor DNBP-1 (human DNMBP) as an in vivo partner of PTPN-22. Consistent with this  
24 interaction, loss of DNBP-1 also suppressed *nekl*-associated molting defects. Genetic analysis,  
25 co-localization studies, and proximity labeling revealed roles for PTPN-22 in several epidermal  
26 adhesion complexes, including *C. elegans* hemidesmosomes, suggesting that PTPN-22 plays a  
27 broad role in maintaining the structural integrity of tissues. Localization and proximity labeling  
28 also implicated PTPN-22 in functions connected to nucleocytoplasmic transport and mRNA  
29 regulation, particularly within the germline, as nearly one-third of proteins identified by PTPN-  
30 22 proximity labeling are known P granule components. Collectively, these studies highlight the  
31 utility of combined genetic and proteomic approaches for identifying novel gene functions.

32

33

## 34 INTRODUCTION

35 Reversible tyrosine phosphorylation is a key mechanism for regulating diverse cellular  
36 processes including differentiation, proliferation, apoptosis, metabolism, and signal  
37 transduction. The steady-state level of tyrosine-phosphorylated proteins is regulated by the  
38 coordinated effects of protein tyrosine kinases (PTKs) and protein tyrosine phosphatases (PTPs).  
39 Of the 518 protein kinases in humans, 90 (17%) are classified as PTKs, whereas of the 200  
40 protein phosphatases, 108 (54%) are classified as PTPs (1–3). Despite their greater abundance,  
41 PTPs have garnered less attention from researchers than PTKs. Nevertheless, it is known that  
42 dysfunction of PTPs can disrupt the homeostasis of tyrosine-phosphorylated proteins,  
43 contributing to a spectrum of disorders including cancers and neuronal and autoimmune  
44 diseases (4–9). Notably, among the 237 protein phosphatases in *C. elegans*, 94 are presumed to  
45 be PTPs and over 50% of *C. elegans* phosphatases have human orthologs (10,11).

46  
47 Protein tyrosine phosphatase non-receptor type (PTPN) is a subset of the PTP family comprising  
48 17 protein tyrosine phosphatases in humans. One well-studied member of this family, PTPN22,  
49 has been investigated primarily in cells of hematopoietic origin including lymphocytes,  
50 monocytes, natural killer cells, and platelets (12–17). Correspondingly, one of the most well-  
51 characterized functions of PTPN22 is the suppression of T-cell activation. In conjunction with C-  
52 terminal Src tyrosine kinase (CSK), PTPN22 is responsible for dephosphorylating T-cell signaling  
53 receptors including LCK, FYN, CD3 $\zeta$ , and ZAP-70 (18,19). Moreover, a missense polymorphism in  
54 PTPN22, which leads to a R620W substitution in the C terminus of PTPN22, is a common risk  
55 factor for multiple autoimmune diseases including type I diabetes mellitus, systemic lupus

56 erythematosus, and rheumatoid arthritis (20–24). PTPN22 expression is also detected in  
57 epithelial, endothelial, muscle, and nervous tissue, suggesting additional roles for this  
58 phosphatase, although it has been less well studied in these contexts (15–17,25,26).  
59  
60 PTPs also contribute to the formation and maintenance of adhesion complexes in human cells.  
61 Several members of the PTPN family including PTPN11, PTP-PEST (PTPN12), and PTPN22 are  
62 recognized as key regulators of integrin function. Integrins are transmembrane  $\alpha\beta$   
63 heterodimeric receptors that connect the extracellular matrix to the actin cytoskeleton, and  
64 their activation is regulated by phosphorylation to control cell movement and adhesion (27–  
65 30). In human T cells, PTPN22 inhibits signaling by integrin subunit alpha L (ITGAL), which is also  
66 known as integrin lymphocyte function-associated antigen 1 (LFA-1), and loss of PTPN22  
67 function results in increased ITGAL-mediated cell adhesion (31). In PTPN22<sup>-/-</sup> mice, regulatory T  
68 cells also exhibit an increase in ITGAL-dependent adhesion, and these mice show an increase in  
69 platelet-specific  $\alpha_{IIb}\beta_3$  integrin activation along with increased platelet spreading and  
70 aggregation (32,33). Together these findings implicate PTPN22 in cell adhesion, although  
71 analogous functions for PTPN22 beyond the immune system remain largely unexplored.  
72  
73 As described below, we identified the *C. elegans* ortholog of PTPN22 in a genetic screen for  
74 genes that affect the *C. elegans* molting process. Molting is an essential developmental process  
75 in nematodes and other members of the ecdysozoan group, allowing for organismal growth and  
76 adaptation to new environments (34). Molting occurs at the termination of each of the four  
77 larval stages (L1–L4), wherein a new cuticle—an apical extracellular matrix surrounding the

78 epidermis—is synthesized and the old cuticle is released. Many different types of proteins have  
79 roles in the molting process including signal transducers, transcriptional regulators, structural  
80 components and modifiers of the cuticle, cell–ECM adhesion complexes, and proteins that  
81 affect membrane trafficking (34–36). Previous work in our laboratory identified two conserved  
82 NIMA-related kinases, NEKL-2 (human NEK8/NEK9) and NEKL-3 (human NEK6/NEK7)  
83 (collectively referred to as the NEKLs)—along with their three ankyrin repeat binding partners,  
84 MLT-2 (human ANKS6), MLT-3 (human ANKS3), and MLT-4 (human INVS) (collectively referred  
85 to as the MLTs)—as being required for molting (37,38).

86

87 Ongoing research continues to uncover the precise mechanisms by which NEKLs and MLTs  
88 affect the molting process in *C. elegans*. Most notably, we have shown that NEKLs and their  
89 human counterparts regulate several aspects of membrane trafficking (39,40). Further insights  
90 into the functions of NEKLs came from the isolation of genetic suppressors of *nekl* molting  
91 defects, which include core components of the endocytic machinery and several closely  
92 associated factors that regulate actin filamentation, including the Rho-family GTPase CDC-42  
93 and its effector SID-3, which is the ortholog of human TNK2 (tyrosine kinase non receptor 2;  
94 also known as ACK1, activated CDC42-associated kinase 1) (40,41). In this study, we identified  
95 mutations affecting PTPN-22, which we showed binds to the Rho-guanine nucleotide exchange  
96 factor (GEF) DNBP-1, loss of which also suppressed *nekl*-associated molting defects. Using  
97 genetic, proteomic, and cell biological approaches, we have implicated PTPN-22 in a range of  
98 functions including effects on epidermal adhesion complexes, cytoskeletal proteins, and

99 potential germline expression functions, thereby expanding substantially on the known  
100 functions of PTPN22 family members.

101

## 102 **RESULTS**

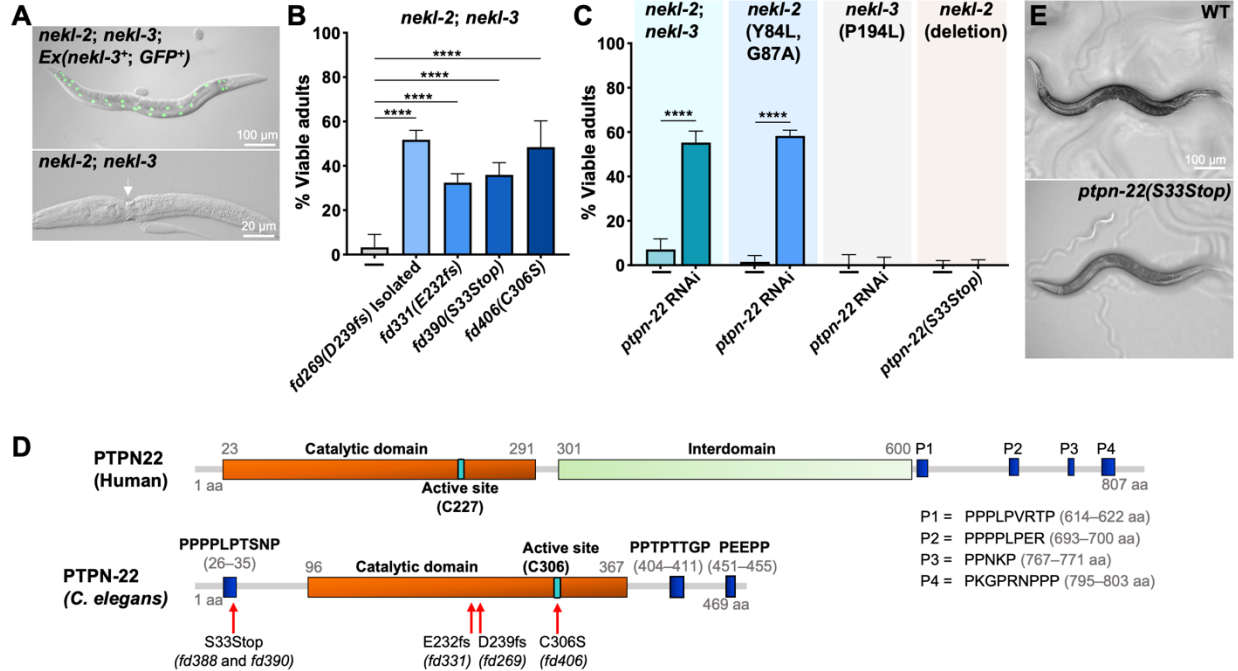
### 103 **Loss of PTPN-22 suppresses molting defects in *nekl* mutants**

104 We previously showed that *nekl-2* and *nekl-3* are required for molting in *C. elegans*, as strong  
105 loss-of-function mutations in either gene cause molting defects in early larval development  
106 (37,38). In contrast, the weak loss-of-function mutations *nekl-2(fd81)* and *nekl-3(gk894345)* do  
107 not exhibit phenotypes individually, but when combined they lead to ~98% of double-mutant  
108 larvae arresting at the L2/L3 molt (Fig 1A and Fig 1B) (37). *nekl-2(fd81); nekl-3(gk894345)*  
109 homozygotes (hereafter referred to as *nekl-2; nekl-3*) can be maintained in the presence of an  
110 extrachromosomal array (*fdEx286*) that contains wild-type copies of *nekl-3* along with a broadly  
111 expressed GFP reporter (*SUR-5::GFP*; Fig 1A) (37).

112

113 To identify proteins that functionally interact with NEKL kinases, we carried out a forward  
114 genetic screen to identify suppressors of molting defects in *nekl-2; nekl-3* mutants (42). From  
115 this screen we identified allele *fd269*, which led to ~50% of *nekl-2; fd269; nekl-3* mutants  
116 reaching adulthood (Fig 1B). Using whole-genome sequencing together with the Sibling  
117 Subtraction Method (42), we identified an insertion in the sixth exon of *ptpn-22* (Y41D4A.5)  
118 that led to a frameshift after D238 of PTPN-22 followed by subsequent stop codons (Fig 1D; S1  
119 File). To determine if the alteration in *ptpn-22* led to *nekl-2; nekl-3* suppression, we used CRISPR  
120 methods to generate a frameshift mutation after L231 (*fd331*) (Fig 1D; S1 File). Likewise, CRISPR

121 Fig 1



122 **Fig 1. Loss of *ptpn-22* can suppress *nekl*-associated molting defects.**  
 123 (A) Merged fluorescence and DIC images of *nekl-2(fd91); nekl-3(gk894345)* worms in the presence (top)  
 124 and absence (bottom) of the extrachromosomal array (*fdEx286*), which contains wild-type *nekl-3* and  
 125 SUR-5::GFP. Note the molting defective *nekl-2; nekl-3* double mutant in the lower panel, which exhibits a  
 126 mid-body constriction due to a failure to shed its old cuticle. (B,C) Bar graphs indicating the percentage  
 127 of worms that developed into viable adults for the indicated genotypes including *ptpn-22* genetic  
 128 mutations and *ptpn-22(RNAi)*. (D) Diagram highlighting the structural features of human PTPN22 and *C.*  
 129 *elegans* PTPN-22 proteins including the catalytic domains (orange), active sites (turquoise), interdomain  
 130 (light green; PTPN22 only), and proline-rich regions (PR.1–3; blue). Amino acid sequences of the proline-  
 131 rich domains are also provided. Also indicated are the locations and effects of *ptpn-22* alleles shown in  
 132 Fig 1B. (E) Bright-field images of a wild-type worm and mutant worm carrying the *ptpn-2(S33Stop)*  
 133 mutation. Error bars represent 95% confidence intervals. Fisher's exact test was used to calculate p-  
 134 values; \*\*\*\*p < 0.0001. Raw data are available in the S7 File. The sequences for *ptpn-22* alleles can be  
 135 found in the S1 File. aa, amino acid.  
 136

137 targeting the N terminus of PTPN-22 yielded a 27-bp insertion in the second exon of PTPN-22,  
138 leading to premature stop codons after position T32 (*fd390*) (Fig 1D; S1 File). Notably, both  
139 mutations induced suppression of *nekl-2*; *nekl-3* mutants, albeit at slightly lower levels than  
140 *fd269* (Fig 1B).

141

142 Additionally, RNA interference (RNAi) of *ptpn-22* using dsRNA injection methods led to ~50%  
143 suppression of *nekl-2*; *nekl-3* lethality, further indicating that loss of PTPN-22 function was  
144 responsible for the suppression of *nekl-2*; *nekl-3* molting defects (Fig 1C). However, whereas  
145 *ptpn-22(RNAi)* effectively suppressed the moderate loss-of-function allele of *nekl-2*, *fd91* (Y84L,  
146 G87A), it failed to suppress molting defects associated with a moderate loss-of-function allele  
147 of *nekl-3*, *sv3* (P194L) (Fig 1C). Furthermore, another CRISPR-generated mutation that led to a  
148 stop codon after T32 (*fd388*) failed to suppress molting defects in a null allele of *nekl-2* (*gk839*)  
149 (Fig 1C). Collectively, our data indicate that loss of *ptpn-22* can suppress weak and some  
150 moderate loss-of-function *nekl* mutations but not strong loss-of-function mutations, a profile  
151 exhibited by several other previously described *nekl* suppressors (40,43,44).

152

153 Human PTPN22 is an 807-amino-acid (aa) protein containing a tyrosine phosphatase catalytic  
154 domain at the N terminus followed by an interdomain and several C-terminal proline-rich  
155 motifs (P1–P4) (Fig 1D) (45). As compared to its human ortholog, *C. elegans* PTPN-22 is  
156 relatively small (469 aa) and contains a single proline-rich region near its N terminus, followed  
157 by the catalytic domain and two additional proline-rich regions in its C terminus (Fig 1D).

158 Sequence alignment between PTPN-22 and orthologs in other organisms indicates conservation

159 primarily within the catalytic domain (S1 Fig); PTPN-22 is 38% identical to human PTPN22 and  
160 59% similar in this region. Transgenic animals carrying only the *ptpn-22(S335Stop)* mutation  
161 exhibit a superficially wild-type phenotype (Fig 1E), indicating that PTPN-22 is not essential  
162 under normal growth conditions. To determine if loss of PTPN-22 catalytic activity is critical for  
163 its suppression of *nekl* molting defects, we mutated the active site cysteine residue (C306),  
164 equivalent to C227 in human PTPN22, using CRISPR/Cas9 methods (18,46). We observed that  
165 *ptpn-22(C306S)* suppressed *nekl-2*; *nekl-3* molting defects by ~50% (Fig 1B), indicating that it is  
166 the loss of PTPN-22 phosphatase activity that leads to the suppression of *nekl-2*; *nekl-3* molting  
167 defects.

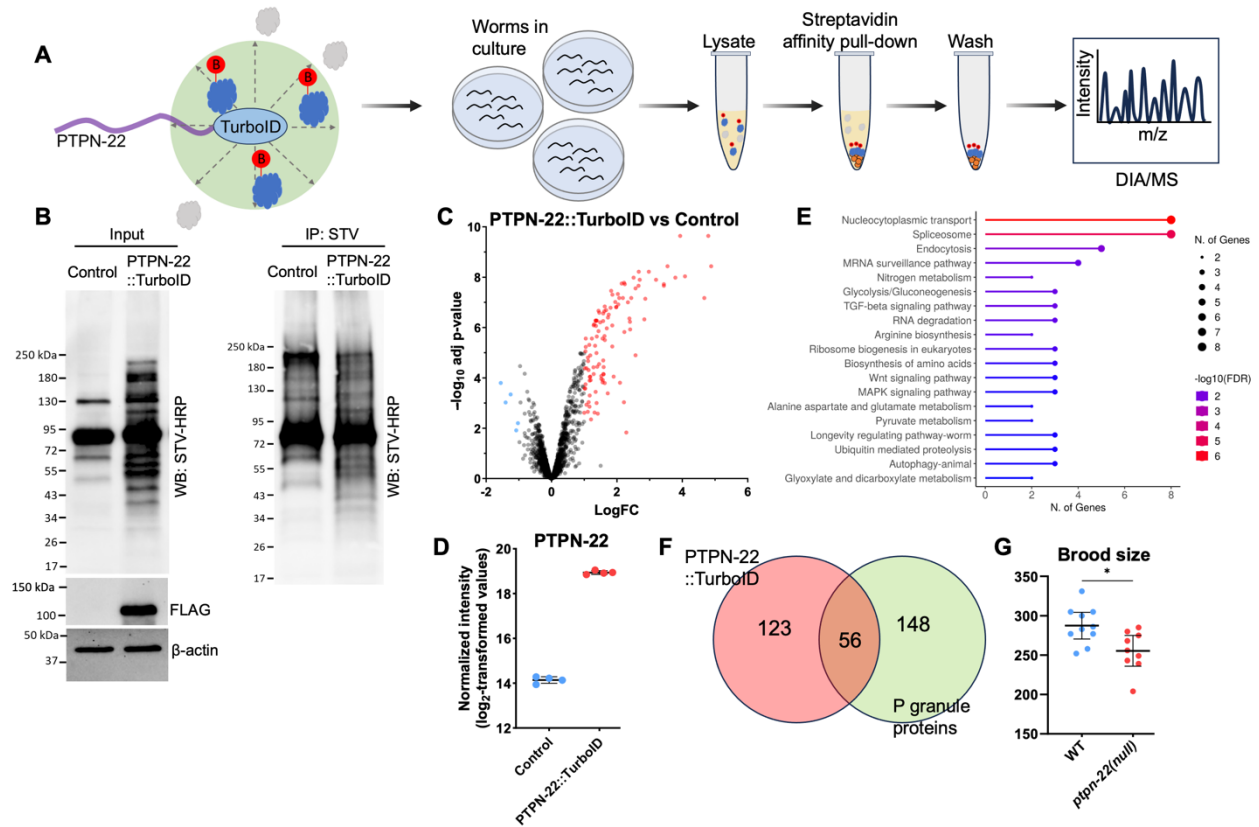
168

#### 169 **Proximity labeling identifies candidate in vivo PTPN-22 interactors**

170 Although mammalian members of the PTPN22 family have been studied extensively in the  
171 context of the adaptive immune system, those findings did not suggest an obvious mechanism  
172 by which *C. elegans* PTPN-22 might functionally interact with NEKL proteins in the context of  
173 molting. We therefore took a non-biased approach to identify potential partners and targets of  
174 *C. elegans* PTPN-22 by mapping its in vivo (proximate) interactome using biotin-based proximity  
175 labeling methods. In proximity labeling, a protein of interest is fused to an *Escherichia coli*-  
176 derived biotin ligase, BirA, and the resulting fusion protein is expressed in cells using either a  
177 native or heterologous promoter. In the presence of ATP, BirA converts non-reactive biotin into  
178 biotinoyl-5'-adenylate, which reacts with lysine residues on nearby (in proximity) proteins to  
179 form covalent linkages to biotin (Fig 2A) (47,48). For our analysis, we used the non-specific  
180 biotin ligase TurboID, an improved version of the BirA enzyme with rapid labeling kinetics,

181  
182

**Fig 2**



**183 Fig 2. TurboID-based proximity labeling identifies the PTPN-22 interactome.**

184 (A) Schematic illustrating the proximity labeling study. The C terminus of PTPN-22 was fused to  
 185 TurboID::3 $\times$ -FLAG, leading to the biotinylation of proximal proteins. Proximal proteins are depicted in  
 186 blue, with the resulting biotin modification highlighted in red, whereas proteins located outside the  
 187 TurboID labeling radius (~10 nm) are represented in gray. PTPN-22::TurboID or N2 control animals were  
 188 cultured on plates, and subsequent protein extraction was carried out. Biotinylated proteins were pulled  
 189 down using streptavidin-coated magnetic beads (orange), whereas non-biotinylated proteins were  
 190 removed through washing steps. Enriched biotinylated proteins were subjected to on-bead digestion,  
 191 followed by Data-Independent Acquisition (DIA) LC-MS/MS analysis. (B) Western blot (WB; left) shows  
 192 the input fractions of representative N2 and PTPN-22::TurboID samples probed with streptavidin-HRP.  
 193 Note additional bands in the PTPN-22::TurboID lysate versus the N2 control. The expression of PTPN-  
 194 22::TurboID was visualized through an anti-FLAG western blot; antibodies against  $\beta$ -actin were used as a  
 195 loading control. The pull-down fraction (IP, right) shows N2 and PTPN-22::TurboID samples probed with  
 196 streptavidin-HRP after enriching for biotinylated proteins using streptavidin-coated beads. (C) Volcano  
 197 plot highlighting proteins enriched (>2-fold and p-value <0.05) in PTPN-22::TurboID samples (red) versus  
 198 N2 (blue). (D) Dot plots show the enrichment of PTPN-22 in PTPN-22::TurboID samples; error bars  
 199 represent standard deviation. (E) KEGG pathway enrichment analysis was performed using ShinyGO 0.80,  
 200 and the top 19 biological pathways based on fold enrichment are shown (114). (F) Venn diagram shows  
 201 the overlap of enriched proteins between PTPN-22::TurboID samples and P granule proteins (S2 File) (G)  
 202 The dot plot shows the brood size of individual worms in the indicated backgrounds  
 203

204 which was fused to the C terminus of PTPN-22 (referred to hereafter as PTPN-22::TurboID)  
205 using CRISPR-based genome editing (49). As our control, we used N2 worms, which lack  
206 TurboID but contain an endogenous specific biotinylation activity that primarily targets four  
207 known carboxylases (MCCC-1, PCCA-1, PYC-1, and POD-2) (49–53).  
208  
209 Four replicates were carried out for both experimental (PTPN-22::TurboID) and control (N2)  
210 strains using mixed-stage worm populations. Crude lysates containing biotinylated proteins  
211 were subjected to pull-down using streptavidin-conjugated beads followed by washing (Fig 2A).  
212 As anticipated, both crude lysates and the corresponding streptavidin-purified samples from N2  
213 and PTPN-22::TurboID exhibited several prominent bands after western blotting that  
214 corresponded to the endogenously biotinylated carboxylases (Fig 2B). Encouragingly, PTPN-  
215 22::TurboID samples also contained numerous additional biotin-positive bands in both input  
216 and pull-down fractions, confirming the functionality of the fused TurboID enzyme (Fig 2B).  
217 Purified samples were subjected to on-bead trypsin digestion followed by liquid  
218 chromatography–tandem mass spectroscopy (LC-MS/MS) analysis using an established data-  
219 independent acquisition pipeline.  
220  
221 We found 112 proteins that were enriched  $\geq 2$ -fold in the PTPN-22::TurboID samples relative to  
222 N2, that were detected in all four PTPN-22::TurboID replicates, and that had adjusted p-values  
223 of  $< 0.05$  (Fig 2C; S2 File; Sheet, “Fold Change  $> 2.0$ ”). Conversely, only five proteins were  
224 enriched in N2 versus PTPN-22::TurboID samples. Moreover, PTPN-22 was the second most  
225 highly enriched protein in the PTPN-22::TurboID samples ( $\sim 28$ -fold) (Fig 2D). In addition, 67

226 proteins were detected in at least three of the four PTPN-22::TurboID replicates but were  
227 undetected in all four N2 control samples (S2 File; Sheet, “ND Control”), leading to a total of  
228 179 proteins that were designated as enriched in PTPN-22::TurboID samples versus N2 (S2 File;  
229 Sheet, “Combined Shortlist”). Estimates suggest that the four biotinylated carboxylases  
230 collectively accounted for ~22% of the proteins identified by LC-MS/MS in the N2 samples and  
231 ~13% in the PTPN-22::TurboID samples, consistent with the enrichment of biotinylated proteins  
232 by the purification process and with the abundance of biotinylated carboxylases in our western  
233 blots relative to PTPN-22::TurboID-specific bands (Fig 2B). These findings further suggest that  
234 the presence of the endogenously biotinylated carboxylases did not substantially affect the  
235 sensitivity of our approach with respect to detecting PTPN-22::TurboID targets.

236

237 False positives in proximity labeling can occur because of non-specific binding by non-  
238 biotinylated proteins to beads and because of non-specific (promiscuous) biotinylation by the  
239 TurboID-tagged proteins themselves. Examples of the latter may occur in cases where non-  
240 specific protein targets are highly abundant, localized within the same compartment(s) as the  
241 protein of interest, and because they are susceptible to biotinylation, such as proteins with  
242 numerous surface-exposed lysine residues (54,55). To address this issue, we cross-referenced  
243 our shortlist of 179 PTPN-22::TurboID hits with data from a previous study by Artan et al. (52) in  
244 which a non-localized GFP::TurboID was expressed at high levels in four different tissues of the  
245 worm (intestine, hypodermis, neurons, and muscle). More specifically, we identified 435  
246 proteins that were among the top 200 most abundant proteins in at least one of the four  
247 tissues and then looked for overlap with our PTPN-22::TurboID dataset (S2 File, Sheet, “Artan

248 Top 200 four tissues”). Among the 112 proteins showing >2-fold enrichment in the PTPN-  
249 22::TurboID study, 62 were also present in the highly enriched dataset; of the 67 proteins in the  
250 “ND Control” dataset, 14 were present in the highly enriched dataset (S2 File, “Artan Overlap”).  
251 Overall, our analysis suggests that although some of the proteins identified by PTPN-  
252 22::TurboID likely represent non-specific targets, many others may correspond to authentic  
253 PTPN-22 proximate proteins.

254

255 Gene ontology analysis of the 179 PTPN-22::TurboID-associated proteins indicated statistically  
256 significant enrichment of proteins acting within various molecular and cellular structures  
257 including the actin cytoskeleton, germline P granules, the NatC/N-terminal protein  
258 acetyltransferase complex, and the spliceosomal small nuclear ribonucleoprotein (snRNP)  
259 complex, among others (S3 File). Enriched biological processes implicated pathways associated  
260 with germline functions, protein transport, mRNA processing and regulation, and several  
261 signaling pathways (Fig 2E; S3 File). Strikingly, of the 179 proximate interactors identified by  
262 PTPN-22::TurboID, 56 (31%) are reported to be components of germline P granules (Fig 2F; S2  
263 File; Sheet, “Overlap with P granules”), RNP condensates that serve as critical regulators of  
264 germline gene expression. Notably, we observed expression of PTPN-22::EGFP in the  
265 perinuclear region of germline cells in a punctate pattern similar to that reported for P granule  
266 proteins (S2 Fig). Consistent with a potential role in the germline, *ptpn-22* mutants had  
267 diminished brood sizes relative to wild type (Fig 2G). Collectively, our proximity labeling findings  
268 implicate PTPN-22 in a diverse range of molecular and tissue-specific functions. This is  
269 consistent with the observed expression of PTPN-22::EGFP and PTPN-22::mScarlet in multiple

270 tissues (S2 Fig and see below) and with RNA expression data available on WormBase, indicating  
271 that PTPN-22 is expressed in multiple tissues throughout development (56).

272

273 Notably, whereas PTPN-22 was broadly expressed, the NEKLs and MLTs are expressed and  
274 required specifically for molting in the hyp7 epidermal syncytium (37–39). To identify PTPN-22–  
275 associated proteins that act within hyp7, we also carried out proximity labeling studies, using  
276 three technical replicates, in which PTPN-22::TurboID was expressed under the control of a  
277 strong hyp7-specific promoter (Y37A1B.5; P<sub>hyp7</sub>::PTPN-22::TurboID) via a multicopy array (S3A  
278 Fig). We validated the functionality of this transgene through western blotting and, as  
279 expected, observed increased levels of biotinylated proteins versus N2 control worms (S3A Fig).  
280 Using the above LC-MS/MS pipeline, we identified 246 proteins that were enriched  $\geq 2$ -fold in  
281 P<sub>hyp7</sub>::PTPN-22::TurboID versus N2 samples, were present in all three P<sub>hyp7</sub>::PTPN-22::TurboID  
282 replicates, and had adjusted p-values of  $< 0.05$ ; three additional proteins were present in all  
283 three P<sub>hyp7</sub>::PTPN-22::TurboID samples but were undetected in all three N2 controls (S3B Fig; S4  
284 File). PTPN-22 was the seventh most enriched protein in the dataset ( $\sim 24$ -fold; S3C Fig) and, as  
285 expected, P<sub>hyp7</sub>::PTPN-22::TurboID hits exhibited minimal overlap with germline-associated  
286 proteins such as P granule components (S3D Fig; S4 File). Similar to our findings for PTPN-  
287 22::TurboID, 62/249 proteins enriched in the P<sub>hyp7</sub>::PTPN-22::TurboID dataset overlapped with  
288 the list of 435 highly abundant biotinylated proteins (S4 File).

289

290 Unlike the PTPN-22::TurboID dataset, however, the volcano plot for P<sub>hyp7</sub>::PTPN-22::TurboID  
291 indicated substantially reduced specificity, given that 193 proteins were upregulated  $\geq 2$ -fold (p

292 <0.05) in N2 versus P<sub>hyp7</sub>::PTPN-22::TurboID samples (compare Fig 2C with S3B Fig). Consistent  
293 with this, the four endogenous carboxylases accounted for only ~3% of total identified proteins  
294 in the P<sub>hyp7</sub>::PTPN-22::TurboID samples and ~13% in the corresponding N2 controls, suggesting  
295 a somewhat higher incidence of non-specific binding by non-biotinylated proteins to the  
296 streptavidin beads. Other differences between the two PTPN-22 proximity labeling experiments  
297 may be due to differences in expression levels and tissues and to additional differences in the  
298 protocols used to enrich for the biotinylated proteins (see Materials and Methods).

299  
300 An analysis of enriched molecular/cellular GO terms in the P<sub>hyp7</sub>::PTPN-22::TurboID dataset  
301 included proteins linked to the actin cytoskeleton, cytoskeletal fibers, and several trafficking  
302 compartments (S5 File). Although only 29 proteins overlapped between the PTPN-22::TurboID  
303 and P<sub>hyp7</sub>::PTPN-22::TurboID shortlists (S3E Fig), these included the actin-capping proteins CAP-  
304 1 and CAP-2, the latter of which genetically interacts strongly with *ptpn-22* (S4 File; Sheet,  
305 “Overlap”; and see below). Collectively, our proximity labeling studies provide a foundation for  
306 uncovering previously unknown molecular and cellular functions and partners of the PTPN-22  
307 family of proteins within the context of an intact developing organism.

308

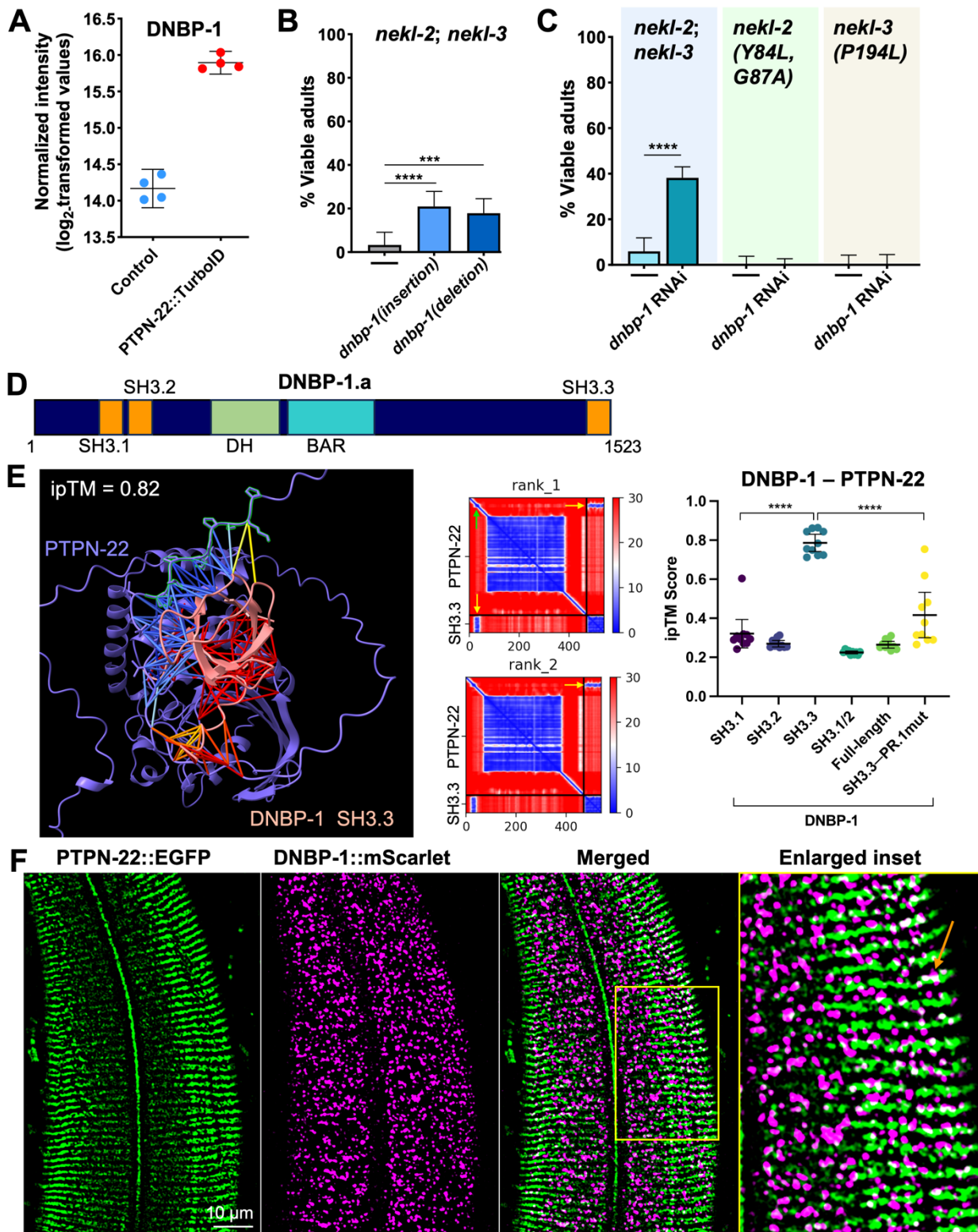
### 309 **DNBP-1 associates with PTPN-22 and is a suppressor of *nekl* molting defects**

310 Given that we identified *ptpn-22* as a suppressor of *nekl* molting defects, we were interested in  
311 identifying proteins that could functionally connect PTPN-22 to the NEKL–MLT pathway.  
312 Interestingly, cross-referencing our list of candidate PTPN-22 interactors with protein–protein  
313 interaction data for PTPN-22 available on WormBase (57) yielded a single hit, DNBP-1 (dynamain

314 binding protein 1), which was enriched ~3.3-fold in all four PTPN-22::TurboID samples (adjusted  
315  $p < 0.0001$ ) (Fig 3A). A prior yeast two-hybrid screen of worm Src homology-3 (SH3) domains  
316 identified a high-confidence interaction between PTPN-22 and the third SH3 domain of DNBP-1  
317 (58). In addition, that screen identified interactions between the first and second SH3 domains  
318 of DNBP-1 with DYN-1 (dynamin), an interaction that is conserved in humans (58–60). We also  
319 note that DNBP-1 was slightly enriched (~1.5-fold) in all three  $P_{\text{hyp7}}::\text{PTPN-22}::\text{TurboID}$  samples,  
320 although this result was not statistically significant (S4 File; Sheet, “Raw Data”).

321  
322 DNBP-1 is an ortholog of human DNMBP/Tuba, which functions as guanine exchange factor  
323 (GEF; i.e., activator) for the Rho-family GTPase CDC-42. Given that we previously showed that  
324 loss of function in CDC-42 and its effector SID-3/TNK2 can suppress *nekl-2*; *nekl-3* molting  
325 defects and that CDC-42 becomes hyperactivated in *nekl* mutants, we hypothesized that the  
326 loss of a CDC-42 activator might similarly alleviate molting defects in *nekl* mutants (41). To test  
327 this, we generated two CRISPR-based loss-of-function alleles of *dnbp-1*. *dnbp-1(fd385)*  
328 introduces a 66-bp insertion into the sixteenth exon of *dnbp-1*, leading to 13 new amino acids  
329 after K913, followed by multiple stop codons (S1 File). *dnbp-1(fd386)* contains a 59-bp deletion  
330 in exon 16, which leads to a frameshift that introduces seven novel amino acids after I915  
331 followed by multiple stop codons (S1 File). Both CRISPR alleles of *dnbp-1* led to ~20%  
332 suppression of molting defects in *nekl-2*; *nekl-3* mutants (Fig 3B). RNAi-mediated knockdown of  
333 DNBP-1 using dsRNA injection methods led to ~40% suppression of molting defects in *nekl-2*;  
334 *nekl-3* mutants (Fig 3C), confirming that it is loss of DNBP-1 activity that confers genetic  
335 suppression. The observed difference in suppression levels between the *dnbp-1* genetic

336 Fig 3



337 **Fig 3. DNBP-1 associates with PTPN-22, and its loss suppresses *nekl* molting defects.**  
 338 (A) Dot plot showing DNBP-1 enrichment in all four PTPN-22::TurboID samples; error bars represent  
 339 standard deviation. (B, C) Bar graphs show the percentage of worms that developed without molting

340 defects in different *nekl* mutants achieved by reducing DNBP-1 activity through either loss-of-function  
341 mutations (B) or RNAi (C). Fisher's exact test was used to calculate p-values; \*\*\*\*p < 0.0001 and \*\*\*p <  
342 0.001. (D) Schematic of DNBP-1A isoform showing structural domains. (E) One of the best predicted  
343 models by AlphaFold-multimer showing the predicted binding interaction between PTPN-22 (in blue)  
344 and the SH3.3 domain of DNBP-1 (in pink) as displayed in ribbon format. The PTPN-22 proline-rich region  
345 is highlighted in green with prolines shown. Colored lines indicate predicted interactions between PTPN-  
346 22 and DNBP-1 within 6 Å. Predicted aligned error (PAE) plots of two of the highest-scoring models  
347 (rank\_1 and rank\_2) of PTPN-22 with the SH3.3 domain of DNBP-1. Yellow arrows indicate the region  
348 corresponding to the predicted interaction; green arrow indicates the PTPN-22 proline-rich region. ipTM  
349 scores for 10 different models (two seeds with six recycles) generated by AlphaFold-multimer were  
350 plotted for the indicated domains of DNBP-1 with full-length wild-type PTPN-22 or PTPN-22 containing a  
351 mutated PR.1 domain (PR.1 mut). Error bars represent 95% confidence intervals; \*\*\*\*p < 0.0001 based  
352 on a t test. (F) Confocal images showing transgenic animals expressing CRISPR-generated PTPN-22::EGFP  
353 (green) and DNBP-1::mScarlet (magenta) in the region of the apical epidermis including inset  
354 (highlighted in yellow box.) The orange arrow indicates an example overlap (white) between PTPN-  
355 22::EGFP and DNBP-1::mScarlet. Sequences for *dnbp-1* mutant alleles can be found in the S1 File. Raw  
356 data are available in the S7 File.  
357  
358  
359

360 mutants and *dnbp-1(RNAi)* may be due in part to a pronounced reduction in fitness caused by  
361 the *dnbp-1* deletion mutation. We note that *dnbp-1(RNAi)* failed to suppress molting defects in  
362 moderate loss-of-function alleles of *nekl-2*(Y84L, G87A) and *nekl-3*(P194L) (Fig 3C). Together  
363 these results identify *dnbp-1* as a novel suppressor of *nekl-2*; *nekl-3* mutants and underscore  
364 the value of proximity labeling for identifying functionally relevant partners for proteins of  
365 interest.

366

367 We next took an in silico approach (AlphaFold-multimer; ColabFold) to better understand how  
368 DNBP-1 and PTPN-22 might physically interact (61,62). The predicted structure of DNBP-1A  
369 isoform (DNBP-1.a) reveals two closely spaced SH3 domains at its N terminus, a Dbl-homology  
370 (DH) domain, a membrane-binding BAR domain, and a third SH3 domain at its C terminus (Fig  
371 3D). As SH3 domains recognize proline-rich motifs, we used AlphaFold-multimer to predict  
372 interactions between DNBP-1 and PTPN-22 using full-length PTPN-22 and individual SH3  
373 domains of DNBP-1 (SH3.1, SH3.2, and SH3.3). According to AlphaFold-multimer predictions, all  
374 10 models suggested strong interactions between the N-terminal proline-rich region (aa 26–35;  
375 PPPPLPTSNP) of PTPN-22 and SH3.3 of DNBP-1 as evidenced by a mean ipTM (for interface  
376 predicted Template Modeling) score of 0.79 (Standard deviation, 0.062; range, 0.71–0.86) (Fig  
377 3E). In contrast, the predicted models suggested a weak interaction or no interactions between  
378 the SH3.1 and SH3.2 domains of DNBP-1 with PTPN-22. Notably, these findings aligned closely  
379 with the yeast two-hybrid screen, which previously identified a physical association specifically  
380 between the SH3.3 domain of DNBP-1 and PTPN-22 (58). Along these lines, both yeast two-  
381 hybrid experiments and protein modeling predicted an interaction between dynamin (DYN-1)

382 and the SH3.1 domain of DNBP-1 (S4A Fig) (58). We note that the failure of AlphaFold-multimer  
383 to predict an interaction between full-length DNBP-1 and PTPN-22 is not unexpected given the  
384 relative lack of confident structural predictions outside of the three SH3 domains (Fig 3E).

385

386 We further carried out co-localization experiments with transgenic animals that expressed  
387 CRISPR (endogenously) tagged PTPN-22::EGFP and DNBP-1::mScarlet. In the epidermis, PTPN-  
388 22::EGFP displayed both diffuse and punctate modes of expression, as well as a stripe-like  
389 assembly pattern along the portion of the apical epidermal surface that overlies the body wall  
390 muscles (Fig 3F). Consistent with an interaction between PTPN-22 and DNBP-1, we observed  
391 some correlation and overlap between the stripe patterns detected using PTPN-22::EGFP and  
392 the punctate structures identified with DNBP-1::mScarlet (Fig 3F and S4B Fig). Nevertheless,  
393 relatively weak expression of PTPN-22::EGFP in other regions of the epidermis made it difficult  
394 to infer the extent of co-localization between these proteins (Fig 3F). We also note that DNBP-  
395 1::mScarlet exhibited a pattern of mid- to large-sized puncta throughout the epidermis, which  
396 are reminiscent of endocytic compartments that co-localize with NEKL kinases as well as with  
397 epidermal CDC-42 (Fig 3F and S4B Fig) (39,41).

398

399 Given indications of a functional interaction between PTPN-22 and DNBP-1, we tested for  
400 genetic interactions between PTPN-22 and DNBP-1 by assaying for potential enhancement of  
401 *nekl-2*; *nekl-3* suppression when both PTPN-22 and DNBP-1 were simultaneously inhibited. Our  
402 results suggested a significant increase in the percentage of suppressed *nekl-2*; *nekl-3* worms  
403 when both PTPN-22 and DNBP-1 were inhibited as compared with the loss of single proteins

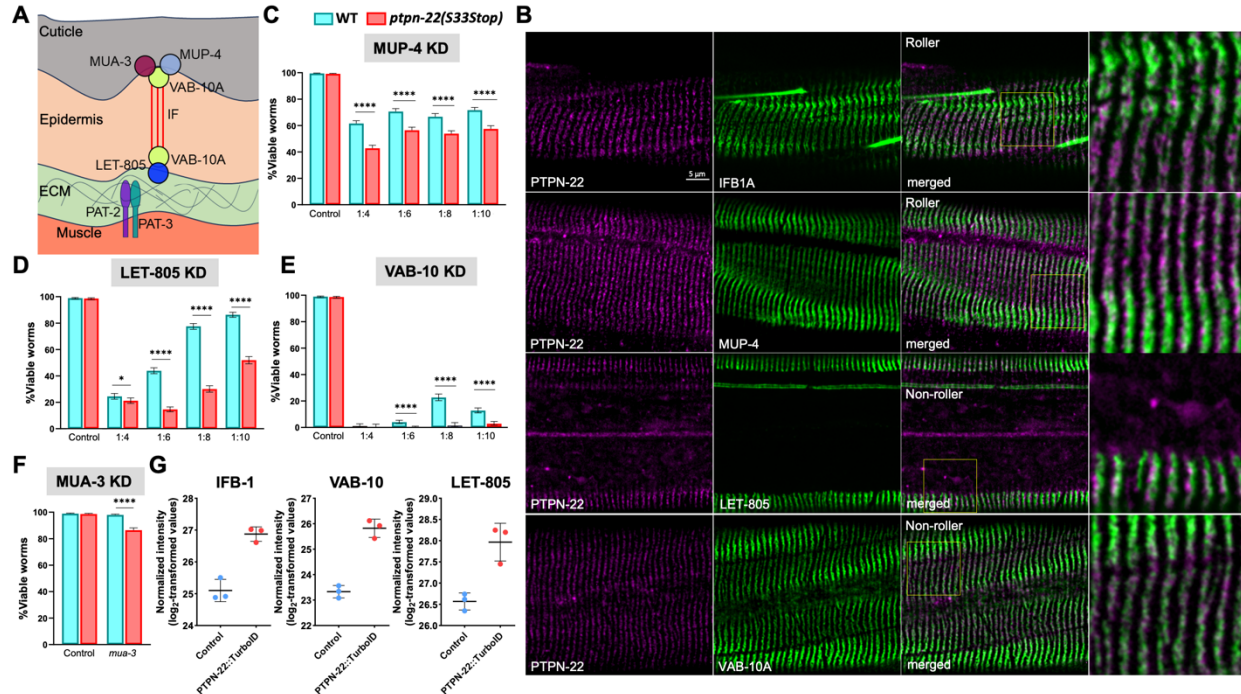
404 including putative null mutations (S4C Fig). Overall, our genetic results suggest that PTPN-22  
405 and DNBP-1 are unlikely to be fully dependent on each other for their activities and also suggest  
406 that PTPN-22 may affect molting through one or more additional targets. Consistent with at  
407 least some functional independence, alteration of the N-terminal proline-rich domain of PTPN-  
408 22 (PR.1; P<sub>26</sub>PPPLPTSNP<sub>35</sub> to AAAALATSNA, referred to as PR.1 mut), which is predicted to  
409 disrupt binding to the SH3.3 domain of DNBP-1, did not lead to strong suppression of *nekl-2*;  
410 *nekl-3* mutants (Fig 3E and S4D Fig). Interestingly, although AlphaFold-multimer predicts that  
411 the P<sub>26</sub>PPPLPTSNP<sub>35</sub> to AAAALATSNA alteration would preclude the binding of the DNBP-1  
412 SH3.3 domain to this sequence, it also predicts that in the absence of the N-terminal proline  
413 rich domain, SH3.3 may instead bind to a C-terminal proline rich region in PTPN-22 (PR.2),  
414 thereby possibly preserving a functional interaction (Fig 3E; S4E Fig). Collectively, our results  
415 indicate a physical and functional connection between DNBP-1 and PTPN-22, although the  
416 regulatory and functional consequences of this interaction remain to be determined.

417

#### 418 **PTPN-22 participates in cell attachment and cytoskeletal regulation**

419 Endogenously tagged PTPN-22::EGFP exhibited an intermittent stripe-like pattern at the apical  
420 surface of hyp7 in the region that overlies body wall muscles (Fig 3F, Fig 4B, and S2 Fig; S1  
421 Movie and S2 Movie). This expression pattern is characteristic of protein components that act  
422 in epidermal–ECM adhesive complexes termed *C. elegans* hemidesmosomes (CeHDs). CeHDs  
423 function to connect body wall muscles to the external cuticle, allowing for movement and  
424 embryonic morphogenesis (63–65). Two epidermal CeHD components related to human  
425 Matrilins, MUP-4 and MUA-3, are transmembrane proteins positioned at the apical end of

426 Fig 4



427 **Fig 4. PTPN-22 is localized to hemidesmosomes and shows a genetic interaction with CeHD proteins.**  
 428 (A) Cartoon illustration depicting apical (MUA-3, MUP-4, and VAB-10A) and basal (LET-805 and VAB-10A)  
 429 CeHD structural components within the epidermis. Intermediate filaments (IFs) connecting the  
 430 complexes are indicated by red lines. The relative sizes of the different layers are not drawn to scale.  
 431 Muscle cells attach to the basal lamina (extracellular matrix, ECM) separating the muscle and epidermis  
 432 via  $\alpha$  and  $\beta$  integrins (PAT-2 and PAT-3, respectively). (B) Co-localization in transgenic worms expressing  
 433 endogenously tagged PTPN-22::mScarlet and GFP-tagged CeHD proteins (IFB-1A::GFP, MUP-4::GFP, LET-  
 434 805::GFP, and VAB-10A::GFP). Note that PTPN-22::mScarlet; IFB-1A::GFP and PTPN-22::mScarlet; MUP-  
 435 4::GFP transgenic worms exhibited a rolling (twisted) phenotype because of the presence of dominant  
 436 *rol-6* (*su1006*) transgene in these backgrounds (see S6 File). (C–F) RNAi feeding knockdown (KD) of *mup-4*  
 437 (C), *let-805* (D), *vab-10* (E), and *mua-3* (F) was carried out in wild-type and *ptpn-22(S33Stop)* worms  
 438 using the indicated dilution series. Error bars represent 95% confidence intervals. Fisher's exact test was  
 439 used to calculate p-values; \*\*\*\* $p < 0.0001$ ; \* $p < 0.05$ . (G) Dot plots show the enrichment of CeHD  
 440 proteins in the P<sub>hyp7</sub>::PTPN-22::TurboID samples. Error bars represent standard deviation. Raw data are  
 441 available in the S7 File.

442  
443

444 CeHDs and interact with the cuticular matrix (66,67). Another epidermal transmembrane CeHD  
445 component, LET-805, is related to human Tenascins and localizes to the basal end of CeHDs  
446 where it interacts with the basement membrane that overlies muscle cells (68). Muscle cells, in  
447 turn, bind to the overlying basement membrane through integrins (PAT-2 and PAT-3) (69–71).  
448 Both MUP-4–MUA-3 and LET-805 bind to VAB-10, a dystonin family member, which in turn  
449 associates with intermediate filaments (IFs), which physically link the apical and basal  
450 complexes (Fig 4A) (66–68,72–75). Interestingly, P<sub>hyp7</sub>::PTPN-22::TurboID proximity labeling  
451 studies indicated enrichment of several CeHD proteins including, LET-805 (~2.6-fold), VAB-10  
452 (~5.6-fold), PAT-12 (~6.0-fold), and IFB-1 (~3.4-fold) (Fig 4G; S4 File).

453  
454 To determine if PTPN-22 co-localizes with CeHDs, we generated a strain expressing  
455 endogenously tagged PTPN-22::mScarlet, which resulted in an expression pattern that closely  
456 resembled that of PTPN-22::EGFP (Fig 3F and Fig 4B). We then tested for co-localization with  
457 (non-CRISPR) GFP-tagged markers of CeHDs including MUP-4::GFP (apical CeHD), VAB-10A::GFP  
458 (apical and basal CeHD), IFB-1::GFP (intermediate filament), and LET-805 (basal CeHD). Our co-  
459 localization studies showed substantial overlap and/or adjacent localization between PTPN-  
460 22::mScarlet stripes and puncta with MUP-4::GFP, VAB-10A::GFP, IFB-1::GFP, and LET-805 (Fig  
461 4B). However, the resolution of confocal microscopy was insufficient to determine the precise  
462 location of PTPN-22 in relation to apical or basal CeHD components.

463  
464 To determine if PTPN-22 affects the function of CeHDs, we carried out partial/weak RNAi  
465 knockdown of several CeHD components in wild type and *ptpn-22* mutants and assayed for

466 developmental defects. Specifically, we used RNAi feeding in conjunction with bacterial dilution  
467 to achieve different levels of target knockdown (see Materials and Methods) and looked for  
468 increased RNAi sensitivity in *ptpn-22* mutants. We note that knockdown of CeHD proteins can  
469 lead to either detachment of the cuticle from the epidermis or detachment of the muscle from  
470 the epidermis, both of which lead to larval arrest and lethality (65–68,72–76). We observed  
471 that loss of function of *ptpn-22* significantly enhanced larval lethality caused by *mup-4(RNAi)* at  
472 multiple dilutions (Fig 4C). Likewise, *ptpn-22* was more sensitive to *let-805(RNAi)* at all dilutions,  
473 leading to an ~3-fold increase in larval lethality at 1:6 and 1:8 dilutions (Fig 4D). In the case of  
474 *vab-10(RNAi)*, we observed significant embryonic lethality at all dilutions, although a substantial  
475 increase in embryonic arrest was observed for *ptpn-22* at 1:8 (~16-fold) and 1:10 (~5-fold)  
476 dilutions versus N2 (Fig 4E). Finally, we observed a small but statistically significant increase in  
477 larval lethality of *ptpn-22* treated with (non-diluted) *mua-3(RNAi)* versus N2 (Fig 4F). Together,  
478 our genetic and localization data suggest that PTPN-22 plays a positive role in the function of *C.*  
479 *elegans* hemidesmosomes. Nevertheless, we failed to detect gross changes in the localization  
480 pattern of CeHD components (MUP-4, IFB-1A, and LET-805) in *ptpn-22* null mutants (S5A Fig),  
481 consistent with the viability and normal morphology of *ptpn-22* mutants. As such, PTPN-22  
482 could play a role in fine-tuning CeHD function, assembly, or stability.

483

484 Given that CeHDs are extensively remodeled during molting cycles, we were curious if loss of  
485 *ptpn-22* might contribute to *nekl* molting suppression in part through its effects on CeHDs in  
486 addition to its implicated interactions with DNBP-1. As a test for this, we carried out partial  
487 RNAi knockdown of the hemidesmosomal proteins *mup-4* and *let-805* in *nekl-2; nekl-3* worms

488 but failed to observe any mitigation of the molting-defective phenotype (S5B Fig). These results  
489 suggest that the role of PTPN-22 at CeHDs may be distinct from functions linked to the NEKL–  
490 MLT pathway.

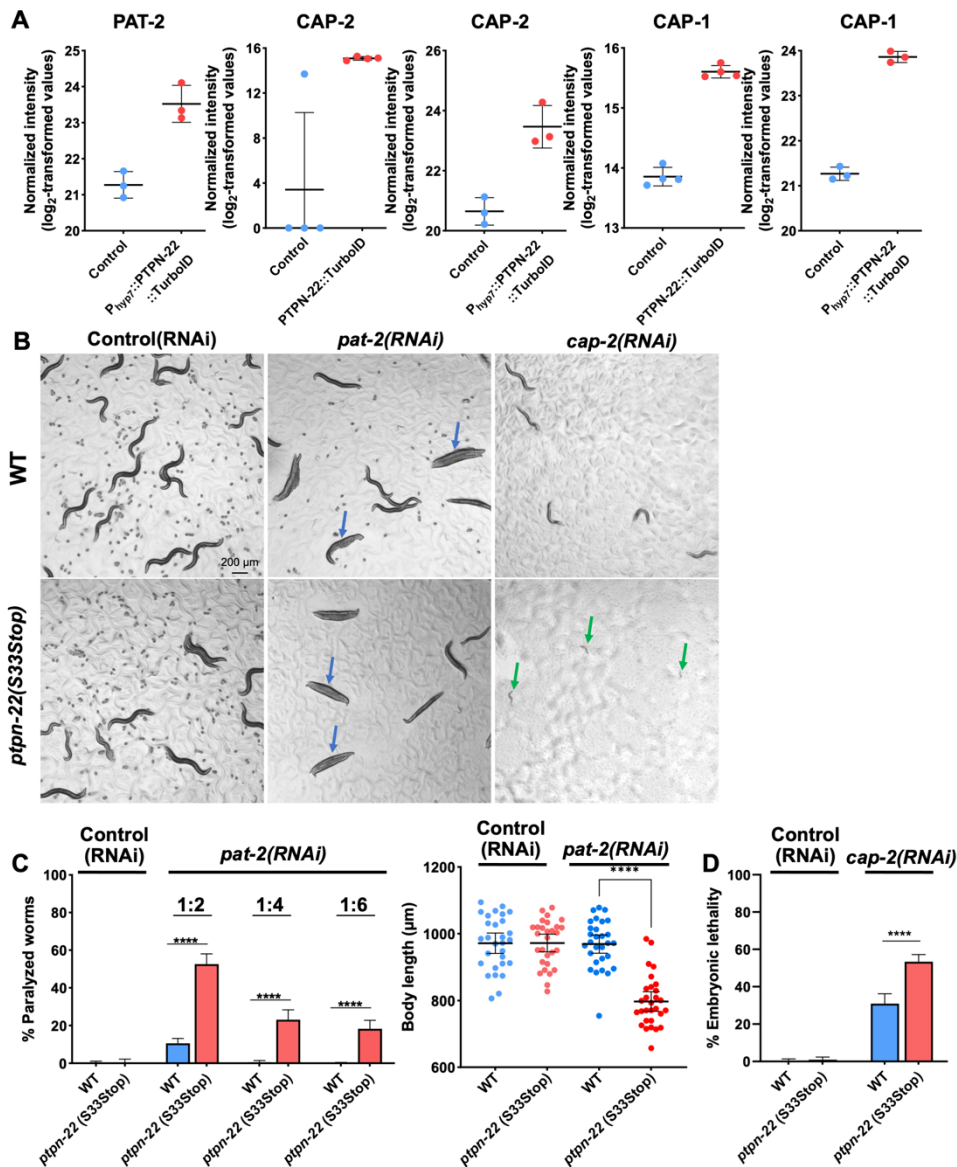
491

492 Previous studies have indicated the involvement of mammalian PTPN22 in suppressing T  
493 lymphocyte-specific integrin activation to regulate integrin-mediated cell adhesion (31,33).  
494 Correspondingly, P<sub>hyp7</sub>::PTPN-22::TurboID proximity labeling studies showed enrichment of the  
495  $\alpha$  subunit of integrin PAT-2/ITGA2B/ITGA5 (~5-fold) and epithelial junction protein DLG-1/DLG1  
496 (~4.3-fold) (Fig 5A and S6A Fig; S4 File) (71,77). To explore a potential role for *C. elegans* PTPN-  
497 22 in integrin function and other adherens junctions beyond CeHDs, we conducted RNAi  
498 enhancement tests to assess *ptpn-22* genetic interactions with *pat-2* and *dlg-1*. *ptpn-22*(S33Stop)  
499 worms had significantly higher paralysis rates when subjected to various dilutions  
500 of *pat-2*(RNAi) feeding treatment as compared with wild-type worms (Fig 5B and Fig 5C).  
501 Interestingly, the combination of *ptpn-22* loss of function and *pat-2*(RNAi) also resulted in a  
502 significant decrease in the size of the worms, as assessed by body length measurements (Fig  
503 5C). Additionally, upon *dlg-1*(RNAi) treatment, *ptpn-22*(S33Stop) worms showed enhanced  
504 embryonic lethality (S6B Fig and S6C Fig). Taken together, these findings suggest that PTPN-22  
505 plays roles in multiple adhesive structures in the epidermis and, potentially, in the muscle.

506

507 Our proximity labeling data also detected enrichment of multiple actin regulatory proteins  
508 including the conserved actin-capping proteins CAP-1/CAPZA1/2, CAP-2/CAPZB, and GSNL-  
509 1/CAPG. CAP-1 and CAP-2 were among the 29 proteins that exhibited enrichment in both PTPN-

510 Fig 5



511 Fig 5. PTPN-22 interactions with cell attachment and actin regulatory proteins.

512 (A) Dot plots showing the enrichment of proteins in the PTPN-22::TurboID and P<sub>hyp7</sub>::PTPN-22::TurboID  
 513 samples. Error bars represent standard deviation. (B) Bright-field images of wild-type and *ptpn-*  
 514 *22*(S33Stop) worms on control (empty vector) or *pat-2* or *cap-2* RNAi feeding plates. Blue arrows  
 515 indicate paralyzed adults; green arrows indicate arrested L1 larvae. (C) Bar graphs show the percentage  
 516 of paralyzed worms in the indicated RNAi feeding experiments. Fisher's exact test was used to calculate  
 517 p-values. Dot plot shows body length measurement of individual worms of the indicated backgrounds on  
 518 control (empty vector) and *pat-2* RNAi feeding plates. Statistical significance was determined using a  
 519 two-tailed, unpaired t-test. Error bars represent 95% confidence intervals. (D) Bar graphs show the  
 520 percentage of embryonic lethality in the indicated RNAi feeding experiments. Fisher's exact test was  
 521 used to calculate p-values. Error bars represent 95% confidence intervals. \*\*\*\*p < 0.0001. Raw data are  
 522 available in the S7 File.

523

524 22::TurboID samples (~4-fold and ~3-fold, respectively) and P<sub>hyp7</sub>::PTPN-22::TurboID samples  
525 (~6-fold and ~7-fold, respectively) (Fig 5A and S3E Fig). GSNL-1 was enriched ~3.2-fold in the  
526 P<sub>hyp7</sub>::PTPN-22::TurboID samples (S6A Fig). Actin-capping proteins maintain the ratio between  
527 globular monomeric actin (G-actin) and filamentous actin (F-actin) by capping the growing end  
528 of actin fibers and have roles in embryonic development and tissue morphogenesis (78–83).  
529 Using our RNAi enhancement approach, we observed that *ptpn-22(S33Stop)* mutants showed  
530 higher embryonic lethality after *cap-2(RNAi)* than wild-type worms (Fig 5B and Fig 5D). In  
531 addition, hatched *ptpn-2(S33Stop); cap-2(RNAi)* worms exhibited uniform early larval arrest,  
532 which was not observed in wild-type worms treated with *cap-2(RNAi)* (Fig 5B). In contrast, no  
533 observable phenotypic defects were detected in either wild-type or *ptpn-22(S33Stop)* worms  
534 when subjected to *gsnl-1(RNAi)* treatment by feeding (S6D Fig). Together, these results  
535 implicate PTPN-22 in the regulation of cell adhesion and the actin cytoskeleton during  
536 development.

537

## 538 DISCUSSION

539 In this study we identified PTPN-22, a conserved tyrosine phosphatase non-receptor type, as an  
540 effector of *C. elegans* molting. Specifically, loss of PTPN-22 catalytic activity alleviated molting  
541 defects in *nekl* mutant backgrounds with partial-to-moderate loss of function. An appealing  
542 model is that the NEKLs and PTPN-22 may exert opposing effects on one or more common  
543 substrates or may act on distinct components within a discrete complex or pathway. Along  
544 those lines, we previously identified a mutation affecting PAA-1/PPP2R1, a conserved  
545 serine/threonine PP2A phosphatase subunit, as a suppressor of *nekl* defects (42). Nevertheless,

546 whereas PP2A could directly reverse NEKL-mediated phosphorylation at serines and threonines,  
547 PTPN-22 is predicted to target specifically phosphotyrosines and may thus oppose NEKL  
548 functions more indirectly.

549

550 We previously showed that NEKL-2 and NEKL-3 have overlapping but distinct roles in several  
551 steps of membrane trafficking including cargo uptake from apical and basolateral membranes  
552 along with transit through the endosomal system (39,40). Additionally, we showed that the  
553 NEKLs inhibit actin filamentation, co-localize at endosomes with CDC-42, and negatively  
554 regulate CDC-42 activity (41). CDC42 is a well-studied member of the Rho family of GTPases  
555 that promotes actin polymerization within a variety of cellular contexts including multiple roles  
556 within the membrane trafficking system. Effectors of CDC42 include conserved members of the  
557 WASP and TOCA family of proteins, which together with the Arp2/3 complex promote the  
558 extension and branching of actin filaments (84–88). CDC42 activity is itself tightly controlled by  
559 upstream regulators including RhoGEFs, such as DNBP-1 family proteins, as well as GTPase-  
560 activating proteins (GAPs). DNMBP, the human ortholog of DNBP-1, regulates actin assembly by  
561 serving as a scaffold for CDC42 and WASP family proteins and also binds to dynamin, a  
562 membrane-remodeling enzyme that promotes vesicle fission (59,60,89). Our findings from  
563 proximity labeling, molecular modeling, and subcellular localization studies, in conjunction with  
564 previously published yeast two-hybrid interaction data, suggest that PTPN-22 may be an  
565 accessory component or regulator of this complex (58). Such a model is consistent with our  
566 current and previously published genetic data showing that inhibition of PTPN-22, DNBP-1,

567 CDC-42, and SID-3/ TNK2/ACK1 can suppress *nekl* molting defects. Nevertheless, the precise  
568 role of PTPN-22 in this context remains to be determined.

569

570 Further examples of the potential involvement of PTPN-22 in actin regulation come from our  
571 proximity labeling experiments, which suggested an interaction between PTPN-22 and several  
572 actin capping proteins (CAP-1, CAP-2, and GSNL-1), each of which blocks actin filament  
573 elongation. Additionally, our genetic experiments revealed a robust genetic interaction  
574 between *cap-2* and *ptpn-22*, as loss of function of both proteins led to a significant increase in  
575 embryonic lethality and developmental arrest at early larval stages. Together these findings  
576 further implicate PTPN-22 in the regulation of actin polymerization.

577

578 PTPN-22 proximity labeling studies also identified several CeHD components (IFB-1, PAT-12,  
579 VAB-10, and LET-805), a finding strongly supported by the observed co-localization between  
580 PTPN-22 and IFB-1A, MUP-4, VAB-10, and LET-805. These results, together with RNAi  
581 enhancement studies showing that *ptpn-22* mutants are hypersensitive to partial knockdown of  
582 CeHD proteins, suggest a role for PTPN-22 in positively regulating the function of CeHD  
583 proteins. Additionally, proximity labeling and genetic interaction studies implicated a  
584 connection between PTPN-22 and PAT-2, a component of the integrin-attachment complex,  
585 and DLG-1, an epithelial junctional protein (65,71,77). As noted in the results, however, our  
586 proximity labeling studies are likely to contain at least some false (non-specific) positives, which  
587 could include highly abundant proteins such as those acting within cell adhesion complexes.  
588 Nevertheless, by coupling proximity labeling to localization data and functional/genetic studies,

589 our combined results indicate functions for PTPN-22 in the regulation of cell attachments and  
590 serve as a basis for future studies. Moreover, previous work on human PTPN22 suggests that  
591 this could be a conserved function given that mammalian PTPN22 co-localizes with a T cell–  
592 specific integrin, regulates its activity, and affects lymphocyte adhesion (31).

593

594 Proximity labeling and PTPN-22 expression studies also implicated PTPN-22 in germline  
595 functions through an apparent connection to P granules. P granules are well-studied RNP-based  
596 membraneless organelles located in the perinuclear region of germline nuclei, where they act  
597 to restrict mRNA cytoplasmic import and protein translation (90–93). Most notably, nearly one-  
598 third of the 179 proteins identified by PTPN-22::TurboID are known P granule components (S2  
599 File; Sheet “Overlap with P granules”). Our results also indicated significant enrichment of  
600 nuclear transport proteins, particularly nuclear pore complex components (NPP-1, NPP-4, NPP-  
601 9, and NPP-14) as well as importins (IMA-2 and IMA-3), in the PTPN-22::TurboID samples (S2  
602 File). P granules are located directly adjacent to nuclear pore complexes, thereby enabling the  
603 rapid sequestration of mRNAs as they pass through nuclear pores (90,94). Additionally, it is  
604 possible that an interaction between PTPN-22, nuclear pore complex proteins, and importins  
605 could occur in other tissues, as we observed expression of PTPN-22 in nuclear compartments of  
606 other cell types including the vulva, pharynx, intestine, and seam cells. Previous studies on the  
607 subcellular localization of human PTPN22 demonstrated expression within the cytoplasm and  
608 nucleus of macrophages and reported distinct functional roles for nuclear and cytoplasmic  
609 PTPN22 (95). Nonetheless, the functions of PTPN22 in nuclear and perinuclear compartments  
610 are poorly understood.

611

612 In summary, our research highlights the value of combining the complementary approaches of  
613 forward genetics and proximity labeling to gain novel insights into gene functions. More  
614 specifically, our studies substantially expand upon the known functions of PTPN22 family  
615 members beyond the adaptive immune system, including evidence for new molecular, cellular,  
616 and developmental functions.

617

## 618 **MATERIALS AND METHODS**

### 619 **Strain maintenance**

620 *C. elegans* strains were maintained using established protocols and cultured at 22°C, unless  
621 otherwise indicated. The strains used in this study are listed in the S6 File.

622

### 623 **Genome editing**

624 Established CRISPR/Cas9 approaches were used for genome editing in *C. elegans* (96). Ape,  
625 CHOPCHOP, and CRISPRcruncher were used for designing guide RNAs and repair templates (97–  
626 101).

627

### 628 **RNAi**

629 dsRNAs corresponding to *ptpn-22* and *dnbp-1* were generated according to standard protocols.  
630 (40,102). dsRNA at a concentration of 500–800 ng/μL was injected into the gonads of day-1  
631 adult worms. The RNAi feeding protocol was adapted from the procedure outlined by Conte et  
632 al. (103). Briefly, six L4-stage worms were transferred to experimental RNAi plates and

633 transferred every 24 hours for two more times onto fresh RNAi plates. Phenotypic defects were  
634 assessed ~72 hours after their initial placement. To quantify embryonic lethality, eggs were  
635 allowed to hatch for 24 hours, after which dead embryos were counted. For the genes *mup-4*,  
636 *let-805*, *vab-10*, and *pat-2* (as shown in Fig 4 and Fig 5), the penetrance of the RNAi phenotypes  
637 was reduced by diluting the bacterial culture with the control (empty vector) RNAi bacterial  
638 culture at different ratios. The RNAi clones used were obtained from the Ahringer library (104).  
639

#### 640 **Pulldown of biotinylated proteins**

641 The protocol for the pulldown of biotinylated proteins was adapted from the protocol  
642 described by Sanchez et. al. (105). Briefly, mixed-stage worms were cultured at 22°C (except for  
643 S3 Fig, where worms were cultured at 25°C). Subsequently, the worms were washed off the  
644 plates with ddH<sub>2</sub>O and washed multiple times with ddH<sub>2</sub>O to eliminate bacteria. Excess water  
645 was carefully removed. One volume of RIPA lysis buffer supplemented with protease inhibitors  
646 (Thermo Fisher, Cat# 78442) was added to the worm pellet. The pellet was then homogenized  
647 using a handheld homogenizer (Huanyu MT-13K-L) for 4 minutes until complete lysis was  
648 achieved, and intact worms were no longer visible. The lysate was then centrifuged twice at  
649 14,000× *g* for 8 minutes, and the supernatant was transferred to a fresh tube after each spin.  
650 Streptavidin-coated magnetic beads (Thermo Fisher, Cat# 65001) were equilibrated by washing  
651 them twice with RIPA lysis buffer. The lysate was added to the beads and gently rotated on a  
652 spinning wheel at room temperature for 1 hour (except for S3 Fig, where the lysate was mixed  
653 with beads at 4°C for 16 hours). The beads were separated from the lysate using a magnetic  
654 stand. The beads were then washed with five buffers to eliminate non-specifically bound

655 proteins as follows: 1× wash with cold RIPA lysis buffer, 1× wash with cold 1 M KCl, 1× wash  
656 with cold 0.1 M Na<sub>2</sub>CO<sub>3</sub>, 1× wash with cold 2 M urea in 10 mM Tris-HCl (pH 8.0), 3× washes with  
657 cold RIPA lysis buffer, and 5× washes with cold 1× PBS. The beads were snap-frozen and stored  
658 at –80°C until ready for on-bead digestion.

659

### 660 **Western blot analysis**

661 Worms were lysed in RIPA buffer containing Tris-HCl (pH 8.0) 50 mM, NaCl 150 mM, SDS 0.2%,  
662 Sodium deoxycholate 0.5%, Triton X-100 1%, and Halt Protease and Phosphatase Inhibitor  
663 Single-Use Cocktail 1× (Thermo Fisher, Cat# 78442). Proteins from the lysates were separated  
664 by SDS-PAGE, transferred to nitrocellulose filters, and immunoblotted with antibodies using  
665 standard methods. Horseradish peroxidase(HRP)–conjugated streptavidin (streptavidin-HRP;  
666 Cat# 3999S) and HRP-conjugated rabbit monoclonal antibody against β-actin (Cat# 5125S) were  
667 obtained from Cell Signaling Technology. HRP-conjugated mouse monoclonal antibody against  
668 FLAG was obtained from GenScript (Cat# A01428).

669

670 To detect biotinylated proteins by western blot methods, 10 μl of beads were mixed with 3×  
671 Laemmli SDS sample buffer and 2 mM biotin, and then boiled at 95°C for 10 minutes. Beads  
672 were pelleted using a magnetic stand and the supernatant was collected for subsequent use in  
673 western blot analysis.

674

### 675 **Mass spectrometry data analysis**

676 Protein samples were reduced, alkylated, and digested on-bead using filter-aided sample  
677 preparation with sequencing-grade modified porcine trypsin (Promega) (106). Briefly, tryptic  
678 peptides were then separated by reversed-phase XSelect CSH C18 2.5- $\mu$ m resin (Waters) on an  
679 in-line 150 x 0.075-mm column using an UltiMate 3000 RSLCnano system (Thermo Fisher).  
680 Peptides were eluted using a 60-minute gradient of buffer A/buffer B from 98:2 to 65:35. Eluted  
681 peptides were ionized by electrospray (2.2 kV) followed by mass spectrometric analysis on an  
682 Orbitrap Exploris 480 mass spectrometer (Thermo Fisher). After data acquisition, data were  
683 searched using an empirically corrected library against the UniProt *Caenorhabditis elegans*  
684 database and a quantitative analysis was performed to obtain a comprehensive proteomic  
685 profile. Spectronaut (Biognosys version 18.5) was used for database search using the directDIA  
686 method (Fig 2). Notably, for S3 Fig, proteins were identified and quantified using EncyclopeDIA  
687 (107) and visualized with Scaffold DIA (Proteome Software, Portland, Oregon, USA) using a 1%  
688 false discovery threshold at both the protein and peptide level. Protein MS2 exclusive intensity  
689 values were assessed for quality using ProteiNorm (108). The data were normalized using VSN  
690 (Fig 2) (109) or cyclic loess (S3 Fig) (110), and were analyzed using proteoDA (111) to perform  
691 statistical analysis using Linear Models for Microarray Data (limma) with empirical Bayes  
692 (eBayes) smoothing to the standard errors (110–112).

693

694 To estimate the proportion of the four biotinylated carboxylases (MCCC-1, PCCA-1, PYC-1, and  
695 POD-2) in the MS samples we first averaged their individual abundance from the technical  
696 replicates (e.g.,  $a_1+a_2+a_3+a_4/4=aa$ ), then converted these values from log<sub>2</sub> scale ( $2^{aa}$ ), and  
697 then summed these four values (carboxylase-total). Likewise, we summed the values for all

698 detected proteins in the sample (all-total). Lastly, we determined the percentage of the  
699 carboxylases in the total sample  $[(\text{carboxylase-total}/\text{all-total}) * 100]$ .

700

### 701 **Image acquisition and image processing**

702 All confocal images were acquired using an Olympus IX83 inverted microscope with a Yokogawa  
703 spinning-disc confocal head. z-Stack images were acquired using a 100 $\times$ , 1.35 N.A. silicone oil  
704 objective. cellSense 3.3 software (Olympus Corporation) was used for image acquisition.

705

706 For colocalization studies, the raw z-stack images were deconvoluted using the Wiener  
707 deconvolution algorithm (cellSense 3.3 software). The desired z-plane was extracted from the  
708 deconvoluted z-stack images for further analysis.

709

### 710 **Statistics**

711 All statistical tests were performed using software from GraphPad Prism following standard  
712 procedures (113).

713

## 714 **FIGURE LEGENDS**

### 715 **Fig 1. Loss of *ptpn-22* can suppress *nekl*-associated molting defects.**

716 (A) Merged fluorescence and DIC images of *nekl-2(fd91); nekl-3(gk894345)* worms in the  
717 presence (top) and absence (bottom) of the extrachromosomal array (*fdEx286*), which contains  
718 wild-type *nekl-3* and SUR-5::GFP. Note the molting defective *nekl-2; nekl-3* double mutant in the  
719 lower panel, which exhibits a mid-body constriction due to a failure to shed its old cuticle. (B,C)

720 Bar graphs indicating the percentage of worms that developed into viable adults for the  
721 indicated genotypes including *ptpn-22* genetic mutations and *ptpn-22(RNAi)*. (D) Diagram  
722 highlighting the structural features of human PTPN22 and *C. elegans* PTPN-22 proteins including  
723 the catalytic domains (orange), active sites (turquoise), interdomain (light green; PTPN22 only),  
724 and proline-rich regions (PR.1–3; blue). Amino acid sequences of the proline-rich domains are  
725 also provided. Also indicated are the locations and effects of *ptpn-22* alleles shown in Fig 1B. (E)  
726 Bright-field images of a wild-type worm and mutant worm carrying the *ptpn-2(S33Stop)*  
727 mutation. Error bars represent 95% confidence intervals. Fisher's exact test was used to  
728 calculate p-values; \*\*\*\*p < 0.0001. Raw data are available in the S7 File. The sequences for  
729 *ptpn-22* alleles can be found in the S1 File. aa, amino acid.

730

731 **Fig 2. TurboID-based proximity labeling identifies the PTPN-22 interactome.**

732 (A) Schematic illustrating the proximity labeling study. The C terminus of PTPN-22 was fused to  
733 TurboID::3×-FLAG, leading to the biotinylation of proximal proteins. Proximal proteins are  
734 depicted in blue, with the resulting biotin modification highlighted in red, whereas proteins  
735 located outside the TurboID labeling radius (~10 nm) are represented in gray. PTPN-22::TurboID  
736 or N2 control animals were cultured on plates, and subsequent protein extraction was carried  
737 out. Biotinylated proteins were pulled down using streptavidin-coated magnetic beads (orange),  
738 whereas non-biotinylated proteins were removed through washing steps. Enriched biotinylated  
739 proteins were subjected to on-bead digestion, followed by Data-Independent Acquisition (DIA)  
740 LC-MS/MS analysis. (B) Western blot (WB; left) shows the input fractions of representative N2  
741 and PTPN-22::TurboID samples probed with streptavidin-HRP. Note additional bands in the

742 PTPN-22::TurboID lysate versus the N2 control. The expression of PTPN-22::TurboID was  
743 visualized through an anti-FLAG western blot; antibodies against  $\beta$ -actin were used as a loading  
744 control. The pull-down fraction (IP, right) shows N2 and PTPN-22::TurboID samples probed with  
745 streptavidin-HRP after enriching for biotinylated proteins using streptavidin-coated beads. (C)  
746 Volcano plot highlighting proteins enriched (>2-fold and p-value <0.05) in PTPN-22::TurboID  
747 samples (red) versus N2 (blue). (D) Dot plots show the enrichment of PTPN-22 in PTPN-  
748 22::TurboID samples; error bars represent standard deviation. (E) KEGG pathway enrichment  
749 analysis was performed using ShinyGO 0.80, and the top 19 biological pathways based on fold  
750 enrichment are shown (114). (F) Venn diagram shows the overlap of enriched proteins between  
751 PTPN-22::TurboID samples and P granule proteins (S2 File) (G) The dot plot shows the brood  
752 size of individual worms in the indicated backgrounds.

753

754 **Fig 3. DNBP-1 associates with PTPN-22, and its loss suppresses *nekl* molting defects.**

755 (A) Dot plot showing DNBP-1 enrichment in all four PTPN-22::TurboID samples; error bars  
756 represent standard deviation. (B, C) Bar graphs show the percentage of worms that developed  
757 without molting defects in different *nekl* mutants achieved by reducing DNBP-1 activity through  
758 either loss-of-function mutations (B) or RNAi (C). Fisher's exact test was used to calculate p-  
759 values; \*\*\*\*p < 0.0001 and \*\*\*p < 0.001. (D) Schematic of DNBP-1A isoform showing structural  
760 domains. (E) One of the best predicted models by AlphaFold-multimer showing the predicted  
761 binding interaction between PTPN-22 (in blue) and the SH3.3 domain of DNBP-1 (in pink) as  
762 displayed in ribbon format. The PTPN-22 proline-rich region is highlighted in green with prolines  
763 shown. Colored lines indicate predicted interactions between PTPN-22 and DNBP-1 within 6 Å.

764 Predicted aligned error (PAE) plots of two of the highest-scoring models (rank\_1 and rank\_2) of  
765 PTPN-22 with the SH3.3 domain of DNBP-1. Yellow arrows indicate the region corresponding to  
766 the predicted interaction; green arrow indicates the PTPN-22 proline-rich region. ipTM scores  
767 for 10 different models (two seeds with six recycles) generated by AlphaFold-multimer were  
768 plotted for the indicated domains of DNBP-1 with full-length wild-type PTPN-22 or PTPN-22  
769 containing a mutated PR.1 domain (PR.1 mut). Error bars represent 95% confidence intervals;  
770 \*\*\*\*p < 0.0001 based on a t test. (F) Confocal images showing transgenic animals expressing  
771 CRISPR-generated PTPN-22::EGFP (green) and DNBP-1::mScarlet (magenta) in the region of the  
772 apical epidermis including inset (highlighted in yellow box.) The orange arrow indicates an  
773 example overlap (white) between PTPN-22::EGFP and DNBP-1::mScarlet. Sequences for *dnbp-1*  
774 mutant alleles can be found in the S1 File. Raw data are available in the S7 File.

775

776 **Fig 4. PTPN-22 is localized to hemidesmosomes and shows a genetic interaction with CeHD**  
777 **proteins.**

778 (A) Cartoon illustration depicting apical (MUA-3, MUP-4, and VAB-10A) and basal (LET-805 and  
779 VAB-10A) CeHD structural components within the epidermis. Intermediate filaments (IFs)  
780 connecting the complexes are indicated by red lines. The relative sizes of the different layers are  
781 not drawn to scale. Muscle cells attach to the basal lamina (extracellular matrix, ECM)  
782 separating the muscle and epidermis via  $\alpha$  and  $\beta$  integrins (PAT-2 and PAT-3, respectively). (B)  
783 Co-localization in transgenic worms expressing endogenously tagged PTPN-22::mScarlet and  
784 GFP-tagged CeHD proteins (IFB-1A::GFP, MUP-4::GFP, LET-805::GFP, and VAB-10A::GFP). Note  
785 that PTPN-22::mScarlet; IFB-1A::GFP and PTPN-22::mScarlet; MUP-4::GFP transgenic worms

786 exhibited a rolling (twisted) phenotype because of the presence of dominant *rol-6* (*su1006*)  
787 transgene in these backgrounds (see S6 File). (C–F) RNAi feeding knockdown (KD) of *mup-4* (C),  
788 *let-805* (D), *vab-10* (E), and *mua-3* (F) was carried out in wild-type and *ptpn-22(S33Stop)* worms  
789 using the indicated dilution series. Error bars represent 95% confidence intervals. Fisher's exact  
790 test was used to calculate p-values; \*\*\*\*p < 0.0001; \*p < 0.05. (G) Dot plots show the  
791 enrichment of CeHD proteins in the P<sub>hyp7</sub>::PTPN-22::TurboID samples. Error bars represent  
792 standard deviation. Raw data are available in the S7 File.

793

794 **Fig 5. PTPN-22 interactions with cell attachment and actin regulatory proteins.**

795 (A) Dot plots showing the enrichment of proteins in the PTPN-22::TurboID and P<sub>hyp7</sub>::PTPN-  
796 22::TurboID samples. Error bars represent standard deviation. (B) Bright-field images of wild-  
797 type and *ptpn-22(S33Stop)* worms on control (empty vector) or *pat-2* or *cap-2* RNAi feeding  
798 plates. Blue arrows indicate paralyzed adults; green arrows indicate arrested L1 larvae. (C) Bar  
799 graphs show the percentage of paralyzed worms in the indicated RNAi feeding experiments.  
800 Fisher's exact test was used to calculate p-values. Dot plot shows body length measurement of  
801 individual worms of the indicated backgrounds on control (empty vector) and *pat-2* RNAi  
802 feeding plates. Statistical significance was determined using a two-tailed, unpaired t-test. Error  
803 bars represent 95% confidence intervals. (D) Bar graphs show the percentage of embryonic  
804 lethality in the indicated RNAi feeding experiments. Fisher's exact test was used to calculate p-  
805 values. Error bars represent 95% confidence intervals. \*\*\*\*p < 0.0001. Raw data are available in  
806 the S7 File.

807

808 **Fig S1. Multiple sequence alignment of *C. elegans* PTPN-22 and its orthologs in other**  
809 **organisms.**

810 Jalview was used to visualize multi-sequence alignments among *C. elegans* PTPN-22, human  
811 PTPN12 and PTPN22, mouse PTPN22 and PTPN18, chicken PTPN12 and PTPN22, and zebrafish  
812 PTPN12 and PTPN22. Conserved residues, based on sequence homology, are highlighted in  
813 purple. A consensus sequence is provided below the sequence alignments.

814

815 **Fig S2. PTPN-22 expression during development.**

816 (A) A confocal microscopy image of the anterior body of a day-1 adult worm expressing PTPN-  
817 22::EGFP. White arrows show examples of PTPN-22::EGFP in pharyngeal cells; white arrowheads  
818 show its expression in nuclear compartments of pharyngeal cells; yellow arrows indicate  
819 autofluorescence of the cuticle. (B) An L2 larva expressing PTPN-22::EGFP. White arrowheads  
820 indicate seams cells, which show expression in their cytoplasm and nuclei; red arrows indicate  
821 nerve cord cells; yellow arrows indicate autofluorescence of the cuticle. (C) Expression of PTPN-  
822 22::EGFP in the germline of an L4-stage worm including nuclear and perinuclear expression as  
823 indicated with red arrowheads; blue arrowhead indicates a distal tip cell; blue bracket indicates  
824 spermatheca; yellow arrows indicate autofluorescence of cuticle. Yellow box corresponds to the  
825 enlarged inset, which shows expression of PTPN-22::EGFP in the perinuclear region of germline  
826 nuclei. (D) Ubiquitous nuclear and cytoplasmic expression of PTPN-22::mScarlet in early  
827 embryonic cells (left), with the DIC (middle) and merged (right) images. (E) Nuclear and  
828 cytoplasmic expression of PTPN-22::mScarlet in vulval cells in an L4-stage worm (white arrows)  
829 with the DIC (middle) and merged (right) images. The green arrows show expression in

830 intestinal nuclei; blue arrows show gut granule autofluorescence; white bracket indicates  
831 proximal somatic gonad cells.

832

833 **Fig S3. Results of  $P_{hyp7}::PTPN-22::TurboID$  studies.**

834 (A) Schematic showing relevant portion of the expression construct used to drive PTPN-

835 22::TurboID in the major hyp7 epidermal syncytium. A *ptpn-22* cDNA was fused to coding

836 sequences for TurboID and a 3×FLAG tag (both placed at the C terminus) and expressed under

837 the control of a hyp7-specific (Y37A1B.5) promoter. Western blot images of representative N2

838 and  $P_{hyp7}::PTPN-22::TurboID$  samples show the biotinylated proteins in the input and pulldown

839 (IP) fraction after blotting with streptavidin-HRP. The lower two blots on the left show

840  $P_{hyp7}::PTPN-22::TurboID$  expression based on an antibody against FLAG (upper) and a loading

841 control with an antibody against  $\beta$ -actin (lower). (B) The volcano plot shows the enrichment of

842 proteins after LC-MS/MS analysis in the  $P_{hyp7}::PTPN-22::TurboID$  samples (red) and in the N2

843 samples (blue). (C) The dot plot shows normalized intensity values of ectopically expressed

844 PTPN-22cd::TurboID::3×FLAG versus the N2 control (three replicates each). Error bars represent

845 standard deviation. (D, E) Venn diagram shows the overlap of enriched proteins between

846  $P_{hyp7}::PTPN-22::TurboID$  samples and P granule proteins (D) and the overlap of enriched

847 proteins between PTPN-22::TurboID samples and  $P_{hyp7}::PTPN-22::TurboID$  samples (E) (see S4

848 File). cd, cDNA; STV, streptavidin.

849

850 **Fig S4. DNBP-1 interactions and expression.**

851 (A) ipTM scores for five different models generated using AlphaFold-multimer, each of which  
852 was used to determine predicted binding between the three SH3 domains (SH3.1, SH3.2, and  
853 SH3.3) of DNBP-1 and two isoforms of DYN-1 (DYN-1.a and DYN-1.b). Error bars represent  
854 standard deviation. PAE plots of the best models for DYN-1.a and DYN-1b interactions with  
855 DNBP-1(SH3.1) are shown with green arrows indicating the predicted proline-rich region of  
856 interaction at the C terminus of DYN-1.a and DYN-1.b. (B) Representative confocal images of  
857 day-1 adult worms expressing DNBP-1::mScarlet in the anterior and posterior side of the  
858 epidermis. (C,D) Bar graph showing the percentage of suppressed worms in the indicated  
859 backgrounds. Error bars represent 95% confidence intervals. Fisher's exact test was used to  
860 calculate p-values; \*\*\*\*p < 0.0001; ns, not significant. (E) PAE plots showing the two highest-  
861 scoring Alphafold2 multimer interactions models (rank\_1 and rank\_2) of PTPN-22(PR.1mut)  
862 with the SH3.3 domain of DNBP-1. Yellow arrows indicate the predicted interacting region. Raw  
863 data are available in S7 File.

864

865 **Fig S5. CeHD protein expression in wild type and *ptpn-22* mutants and genetic interactions of**  
866 **CeHD proteins with *nekl-2*; *nekl-3* mutants.**

867 (A) Confocal microscopy images of day-1 adults of the indicated backgrounds expressing MUP-  
868 4::GFP, IFB1A::GFP, and LET-805::GFP. Note that no gross differences in the localization of CeHD  
869 proteins were detected. (B) RNAi-suppression experiments were carried out with wild-type and  
870 *nekl-2*; *nekl-3* mutants after partial knockdown of *mup-4* and *let-805* using RNAi feeding at  
871 different dilutions (see Materials and Methods). Note that no reduction in the percentage of

872 *nekl-2*; *nekl-3* arrest was observed. Error bars represent 95% confidence intervals. Fisher's exact  
873 test was used to calculate p-values; ns, not significant. Raw data are available in the S7 File.

874

875 **Fig S6. PTPN-22 interaction with PAT-2 and actin-capping proteins.**

876 (A) Dot plots show the enrichment of the indicated proteins in the N2 and P<sub>hyp7</sub>::PTPN-  
877 22::TurboID samples. (B) Bright-field images of wild-type and *ptpn-22(S33Stop)* worms on  
878 control (empty vector) or *dlg-1* RNAi feeding plates. Red arrow shows the presence of dead  
879 eggs on the *dlg-1(RNAi)* plate. (C, D) Bar graphs show the percentage of embryonic lethality (C)  
880 and viable adults (D) of the indicated backgrounds in control (empty vector) and *gsnl-1* RNAi  
881 feeding plates. Raw data are available in S7 File.

882

883

884 **ACKNOWLEDGEMENTS**

885 We thank Amy Fluet for editing this manuscript. This work was supported by R35 GM136236  
886 and by an Institutional Development Award (IDeA) from the National Institute of General  
887 Medical Sciences of the National Institutes of Health (2P20GM103432). We also thank  
888 Stephanie Byrum and the IDeA National Resource for Quantitative Proteomics (NIH/NIGMS  
889 grant- R24GM137786) for proteomic analyses and helpful discussions.

890

891 **REFERENCES**

- 892 1. Manning G, Whyte DB, Martinez R, Hunter T, Sudarsanam S. The protein kinase  
893 complement of the human genome. *Science* [Internet]. 2002 Dec 6;298(5600):1912–34.  
894 Available from: <http://www.ncbi.nlm.nih.gov/pubmed/12471243>
- 895 2. Aschner Y, Downey GP. The importance of tyrosine phosphorylation control of cellular  
896 signaling pathways in respiratory disease: pY and pY not. Vol. 59, *American Journal of*  
897 *Respiratory Cell and Molecular Biology*. American Thoracic Society; 2018. p. 535–47.
- 898 3. Sacco F, Perfetto L, Castagnoli L, Cesareni G. The human phosphatase interactome: An  
899 intricate family portrait. Vol. 586, *FEBS Letters*. 2012. p. 2732–9.
- 900 4. Zhao X, Xiong L, She L, Li L, Huang P, Liang G. The role and therapeutic implication of  
901 protein tyrosine phosphatases in Alzheimer’s disease. Vol. 151, *Biomedicine and*  
902 *Pharmacotherapy*. Elsevier Masson s.r.l.; 2022.
- 903 5. Shu L, Du C, Zuo Y. Abnormal phosphorylation of protein tyrosine in neurodegenerative  
904 diseases. Vol. 82, *Journal of Neuropathology and Experimental Neurology*. Oxford  
905 University Press; 2023. p. 826–35.
- 906 6. Labbé DP, Hardy S, Tremblay ML. Protein tyrosine phosphatases in cancer: Friends and  
907 foes! In: *Progress in Molecular Biology and Translational Science*. Elsevier B.V.; 2012. p.  
908 253–306.
- 909 7. Sivaganesh V, Sivaganesh V, Scanlon C, Iskander A, Maher S, Lê T, et al. Protein tyrosine  
910 phosphatases: Mechanisms in cancer. Vol. 22, *International Journal of Molecular*  
911 *Sciences*. MDPI; 2021.
- 912 8. Vang T, Miletic A V., Arimura Y, Tautz L, Rickert RC, Mustelin T. Protein tyrosine  
913 phosphatases in autoimmunity. Vol. 26, *Annual Review of Immunology*. 2008. p. 29–55.
- 914 9. Tonks NK. Protein tyrosine phosphatases: from genes, to function, to disease. *Nat Rev*  
915 *Mol Cell Biol* [Internet]. 2006 Nov;7(11):833–46. Available from:  
916 <http://www.ncbi.nlm.nih.gov/pubmed/17057753>
- 917 10. Bye-A-Jee H, Zaru R, Magrane M, Orchard S. Caenorhabditis elegans phosphatase  
918 complexes in UniProtKB and Complex Portal. Vol. 287, *FEBS Journal*. Blackwell Publishing  
919 Ltd; 2020. p. 2664–84.
- 920 11. Kim W, Underwood RS, Greenwald I, Shaye DD. Ortholist 2: A new comparative genomic  
921 analysis of human and caenorhabditis elegans genes. *Genetics*. 2018 Oct 1;210(2):445–  
922 61.
- 923 12. Cohen S, Dadi H, Shaoul E, Sharfe N, Roifman CM. Cloning and characterization of a  
924 lymphoid-specific, inducible human protein tyrosine phosphatase, Lyp. *Blood* [Internet].  
925 1999 Mar 15;93(6):2013–24. Available from:  
926 <http://www.ncbi.nlm.nih.gov/pubmed/10068674>
- 927 13. Hill RJ, Zozulya S, Lu YL, Ward K, Gishizky M, Jallal B. The lymphoid protein tyrosine  
928 phosphatase Lyp interacts with the adaptor molecule Grb2 and functions as a negative  
929 regulator of T-cell activation. Vol. 30, *Experimental Hematology*. 2002.
- 930 14. Cloutier JF, Veillette A. Association of inhibitory tyrosine protein kinase p50csk with  
931 protein tyrosine phosphatase PEP in T cells and other hemopoietic cells. *EMBO J*  
932 [Internet]. 1996 Sep 16;15(18):4909–18. Available from:  
933 <http://www.ncbi.nlm.nih.gov/pubmed/8890164>
- 934 15. Xue C, Jiang L, Zhou M, Long Q, Chen Y, Li X, et al. PCGA: a comprehensive web server for  
935 phenotype-cell-gene association analysis. *Nucleic Acids Res*. 2022 Jul 5;50(W1):W568–76.

- 936 16. Thul PJ, Akesson L, Wiking M, Mahdessian D, Geladaki A, Ait Blal H, et al. A subcellular  
937 map of the human proteome. *Science* (1979). 2017 May 26;356(6340).
- 938 17. Uhlén M, Fagerberg L, Hallström BM, Lindskog C, Oksvold P, Mardinoglu A, et al. Tissue-  
939 based map of the human proteome. *Science* (1979). 2015 Jan 23;347(6220).
- 940 18. Wu J, Katrekar A, Honigberg LA, Smith AM, Conn MT, Tang J, et al. Identification of  
941 substrates of human protein-tyrosine phosphatase PTPN22. *Journal of Biological*  
942 *Chemistry*. 2006 Apr 21;281(16):11002–10.
- 943 19. Cloutier JF, Veillette A. Cooperative inhibition of T-cell antigen receptor signaling by a  
944 complex between a kinase and a phosphatase. *J Exp Med* [Internet]. 1999 Jan  
945 4;189(1):111–21. Available from: <http://www.ncbi.nlm.nih.gov/pubmed/9874568>
- 946 20. Zheng J, Ibrahim S, Petersen F, Yu X. Meta-analysis reveals an association of PTPN22  
947 C1858T with autoimmune diseases, which depends on the localization of the affected  
948 tissue. *Genes Immun*. 2012 Dec;13(8):641–52.
- 949 21. Bottini N, Musumeci L, Alonso A, Rahmouni S, Nika K, Rostamkhani M, et al. A functional  
950 variant of lymphoid tyrosine phosphatase is associated with type I diabetes. *Nat Genet*.  
951 2004 Apr;36(4):337–8.
- 952 22. Kyogoku C, Langefeld CD, Ortmann WA, Lee A, Selby S, Carlton VEH, et al. Genetic  
953 association of the R620W polymorphism of protein tyrosine phosphatase PTPN22 with  
954 human SLE. *Am J Hum Genet* [Internet]. 2004 Sep;75(3):504–7. Available from:  
955 <http://www.ncbi.nlm.nih.gov/pubmed/15273934>
- 956 23. Begovich AB, Carlton VEH, Honigberg LA, Schrodi SJ, Chokkalingam AP, Alexander HC, et  
957 al. A missense single-nucleotide polymorphism in a gene encoding a protein tyrosine  
958 phosphatase (PTPN22) is associated with rheumatoid arthritis. *Am J Hum Genet*  
959 [Internet]. 2004 Aug;75(2):330–7. Available from:  
960 <http://www.ncbi.nlm.nih.gov/pubmed/15208781>
- 961 24. Anderson W, Barahmand-Pour-whitman F, Linsley PS, Cerosaletti K, Buckner JH, Rawlings  
962 DJ. PTPN22 R620W gene editing in T cells enhances low-avidity TCR responses. *Elife*.  
963 2023;12.
- 964 25. Sjöstedt E, Zhong W, Fagerberg L, Karlsson M, Mitsios N, Adori C, et al. An atlas of the  
965 protein-coding genes in the human, pig, and mouse brain. *Science*. 2020 Mar  
966 6;367(6482).
- 967 26. Karlsson M, Zhang C, Méar L, Zhong W, Digre A, Katona B, et al. A single-cell type  
968 transcriptomics map of human tissues. *Sci Adv*. 2021 Jul;7(31).
- 969 27. Sallee JL, Wittchen ES, Burridge K. Regulation of cell adhesion by protein-tyrosine  
970 phosphatases II. Cell-cell adhesion. Vol. 281, *Journal of Biological Chemistry*. 2006. p.  
971 16189–92.
- 972 28. Burridge K, Sastry SK, Sallee JL. Regulation of cell adhesion by protein-tyrosine  
973 phosphatases: I. Cell-matrix adhesion. Vol. 281, *Journal of Biological Chemistry*. 2006. p.  
974 15593–6.
- 975 29. Young KA, Biggins L, Sharpe HJ. Protein tyrosine phosphatases in cell adhesion. Vol. 478,  
976 *Biochemical Journal*. Portland Press Ltd; 2021. p. 1061–83.
- 977 30. Gahmberg CG, Grönholm M. How integrin phosphorylations regulate cell adhesion and  
978 signaling. Vol. 47, *Trends in Biochemical Sciences*. Elsevier Ltd; 2022. p. 265–78.

- 979 31. Burn GL, Cornish GH, Potrzebowska K, Samuelsson M, Griffié J, Minoughan S, et al.  
980 Superresolution imaging of the cytoplasmic phosphatase PTPN22 links integrin-mediated  
981 T cell adhesion with autoimmunity. *Sci Signal*. 2016 Oct 4;9(448).
- 982 32. Wang X, Wei G, Ding Y, Gui X, Tong H, Xu X, et al. Protein tyrosine phosphatase PTPN22  
983 negatively modulates platelet function and thrombus formation. *Blood* [Internet]. 2022  
984 Sep 1 [cited 2023 Dec 6];140(9):1038–51. Available from:  
985 <http://www.ncbi.nlm.nih.gov/pubmed/35767715>
- 986 33. Brownlie RJ, Miosge LA, Vassilakos D, Svensson LM, Cope A, Zamoyska R. Lack of the  
987 phosphatase PTPN22 increases adhesion of murine regulatory T cells to improve their  
988 immunosuppressive function. *Sci Signal*. 2012 Nov 27;5(252).
- 989 34. Lažetić V, Fay DS. Molting in *C. elegans*. *Worm* [Internet]. 2017 Jan 2;6(1):e1330246.  
990 Available from: <http://www.ncbi.nlm.nih.gov/pubmed/28702275>
- 991 35. Miao R, Li M, Zhang Q, Yang C, Wang X. An ECM-to-Nucleus Signaling Pathway Activates  
992 Lysosomes for *C. elegans* Larval Development. *Dev Cell*. 2020 Jan 6;52(1):21-37.e5.
- 993 36. Frand AR, Russel S, Ruvkun G. Functional genomic analysis of *C. elegans* molting. *PLoS*  
994 *Biol*. 2005 Oct;3(10):e312.
- 995 37. Lažetić V, Fay DS. Conserved ankyrin repeat proteins and their NIMA kinase partners  
996 regulate extracellular matrix remodeling and intracellular trafficking in *Caenorhabditis*  
997 *elegans*. *Genetics*. 2017 Jan 1;205(1):273–93.
- 998 38. Yochem J, Lažetić V, Bell L, Chen L, Fay D. *C. elegans* NIMA-related kinases NEKL-2 and  
999 NEKL-3 are required for the completion of molting. *Dev Biol*. 2015 Feb 15;398(2):255–66.
- 1000 39. Joseph BB, Naslavsky N, Binti S, Conquest S, Robison L, Bai G, et al. Conserved NIMA  
1001 kinases regulate multiple steps of endocytic trafficking. *PLoS Genet* [Internet]. 2023 Apr  
1002 1;19(4):e1010741. Available from: <http://www.ncbi.nlm.nih.gov/pubmed/37099601>
- 1003 40. Joseph BB, Wang Y, Edeen P, Lazetic V, Grant BD, Fay DS. Control of clathrin-mediated  
1004 endocytosis by NIMA family kinases. *PLoS Genet*. 2020;16(2).
- 1005 41. Lažetić V, Joseph BB, Bernazzani SM, Fay DS. Actin organization and endocytic trafficking  
1006 are controlled by a network linking NIMA-related kinases to the CDC-42-SID-3/ACK1  
1007 pathway. *PLoS Genet*. 2018 Apr 1;14(4).
- 1008 42. Joseph BB, Blouin NA, Fay DS. Use of a sibling subtraction method for identifying causal  
1009 mutations in *Caenorhabditis elegans* by whole-genome sequencing. *G3: Genes,*  
1010 *Genomes, Genetics*. 2018 Feb 1;8(2):669–78.
- 1011 43. Joseph BB, Edeen PT, Meadows S, Binti S, Fay DS. An unexpected role for the conserved  
1012 ADAM-family metalloprotease ADM-2 in *Caenorhabditis elegans* molting. *PLoS Genet*.  
1013 2022 May 31;18(5).
- 1014 44. Binti S, Melinda R V., Joseph BB, Edeen PT, Miller SD, Fay DS. A life cycle alteration can  
1015 correct molting defects in *Caenorhabditis elegans*. *Dev Biol*. 2022 Mar 1;483:143–56.
- 1016 45. Bottini N, Peterson EJ. Tyrosine phosphatase PTPN22: Multifunctional regulator of  
1017 immune signaling, development, and disease. Vol. 32, *Annual Review of Immunology*.  
1018 Annual Reviews Inc.; 2014. p. 83–119.
- 1019 46. Flint AJ, Tiganis T, Barford D, Tonks NK. Development of “substrate-trapping” mutants to  
1020 identify physiological substrates of protein tyrosine phosphatases. *Proc Natl Acad Sci U S*  
1021 *A* [Internet]. 1997 Mar 4;94(5):1680–5. Available from:  
1022 <http://www.ncbi.nlm.nih.gov/pubmed/9050838>

- 1023 47. Eisenberg MA, Prakash O, Hsiung SC. Purification and properties of the biotin repressor.  
1024 A bifunctional protein. *Journal of Biological Chemistry*. 1982;257(24):15167–73.
- 1025 48. Barker DF, Campbell AM. Genetic and biochemical characterization of the birA gene and  
1026 its product: evidence for a direct role of biotin holoenzyme synthetase in repression of  
1027 the biotin operon in *Escherichia coli*. *J Mol Biol [Internet]*. 1981 Mar 15;146(4):469–92.  
1028 Available from: <http://www.ncbi.nlm.nih.gov/pubmed/6456358>
- 1029 49. Branon TC, Bosch JA, Sanchez AD, Udeshi ND, Svinkina T, Carr SA, et al. Efficient  
1030 proximity labeling in living cells and organisms with TurboID. *Nat Biotechnol*. 2018 Oct  
1031 1;36(9):880–98.
- 1032 50. Price IF, Hertz HL, Pastore B, Wagner J, Tang W. Proximity labeling identifies LOTUS  
1033 domain proteins that promote the formation of perinuclear germ granules in *C. elegans*.  
1034 *Elife [Internet]*. 2021 Nov 3;10. Available from:  
1035 <http://www.ncbi.nlm.nih.gov/pubmed/34730513>
- 1036 51. Holzer E, Rumpf-Kienzl C, Falk S, Dammermann A. A modified TurboID approach  
1037 identifies tissue-specific centriolar components in *C. elegans*. *PLoS Genet*. 2022 Apr  
1038 20;18(4).
- 1039 52. Artan M, Barratt S, Flynn SM, Begum F, Skehel M, Nicolas A, et al. Interactome analysis of  
1040 *Caenorhabditis elegans* synapses by TurboID-based proximity labeling. *Journal of*  
1041 *Biological Chemistry*. 2021 Sep 1;297(3).
- 1042 53. Artan M, Hartl M, Chen W, de Bono M. Depletion of endogenously biotinylated  
1043 carboxylases enhances the sensitivity of TurboID-mediated proximity labeling in  
1044 *Caenorhabditis elegans*. *Journal of Biological Chemistry*. 2022 Sep 1;298(9).
- 1045 54. Bosch JA, Chen CL, Perrimon N. Proximity-dependent labeling methods for proteomic  
1046 profiling in living cells: An update. *Wiley Interdiscip Rev Dev Biol*. 2021 Jan;10(1):e392.
- 1047 55. Moreira CM do N, Kelemen CD, Obado SO, Zahedifard F, Zhang N, Holetz FB, et al. Impact  
1048 of inherent biases built into proteomic techniques: Proximity labeling and affinity capture  
1049 compared. *J Biol Chem*. 2023 Jan;299(1):102726.
- 1050 56. Davis P, Zarowiecki M, Arnaboldi V, Becerra A, Cain S, Chan J, et al. WormBase in 2022–  
1051 data, processes, and tools for analyzing *Caenorhabditis elegans*. *Genetics*. 2022 Apr  
1052 1;220(4).
- 1053 57. Davis P, Zarowiecki M, Arnaboldi V, Becerra A, Cain S, Chan J, et al. WormBase in 2022—  
1054 data, processes, and tools for analyzing *Caenorhabditis elegans*. *Genetics*. 2022 Apr  
1055 4;220(4).
- 1056 58. Xin X, Gfeller D, Cheng J, Tonikian R, Sun L, Guo A, et al. SH3 interactome conserves  
1057 general function over specific form. *Mol Syst Biol*. 2013;9.
- 1058 59. Cestra G, Kwiatkowski A, Salazar M, Gertler F, De Camilli P. Tuba, a GEF for CDC42, links  
1059 dynamin to actin regulatory proteins. *Methods Enzymol*. 2005;404:537–45.
- 1060 60. Salazar MA, Kwiatkowski A V., Pellegrini L, Cestra G, Butler MH, Rossman KL, et al. Tuba,  
1061 a novel protein containing bin/amphiphysin/Rvs and Dbl homology domains, links  
1062 dynamin to regulation of the actin cytoskeleton. *J Biol Chem*. 2003;278(49):49031–43.
- 1063 61. Evans R, O’neill M, Pritzel A, Antropova N, Senior A, Green T, et al. Protein complex  
1064 prediction with AlphaFold-Multimer. 2022; Available from:  
1065 <https://doi.org/10.1101/2021.10.04.463034>

- 1066 62. Mirdita M, Schütze K, Moriwaki Y, Heo L, Ovchinnikov S, Steinegger M. ColabFold: making  
1067 protein folding accessible to all. *Nat Methods*. 2022 Jun;19(6):679–82.
- 1068 63. Zhang H, Labouesse M. The making of hemidesmosome structures in vivo. Vol. 239,  
1069 *Developmental Dynamics*. 2010. p. 1465–76.
- 1070 64. Cox EA, Hardin J. Sticky worms: Adhesion complexes in *C. elegans*. *J Cell Sci*. 2004 Apr  
1071 15;117(10):1885–97.
- 1072 65. Pásti G, Labouesse M. Epithelial junctions, cytoskeleton, and polarity. *WormBook : the*  
1073 *online review of C. elegans biology*. 2014. p. 1–35.
- 1074 66. Hong L, Elbl T, Ward J, Franzini-Armstrong C, Rybicka KK, Gatewood BK, et al. MUP-4 is a  
1075 novel transmembrane protein with functions in epithelial cell adhesion in *Caenorhabditis*  
1076 *elegans*. *Journal of Cell Biology*. 2001 Jul 23;154(2):403–14.
- 1077 67. Bercher M, Wahl J, Vogel BE, Lu C, Hedgecock EM, Hall DH, et al. *mua-3*, a gene required  
1078 for mechanical tissue integrity in *Caenorhabditis elegans*, encodes a novel  
1079 transmembrane protein of epithelial attachment complexes. *Journal of Cell Biology*. 2001  
1080 Jul 23;154(2):415–26.
- 1081 68. Hresko MC, Schriefer LA, Shrimankar P, Waterston RH. Myotactin, a Novel Hypodermal  
1082 Protein Involved in Muscle–Cell Adhesion in *Caenorhabditis elegans*. *J Cell Biol* [Internet].  
1083 1999 Aug 9;146(3):659–72. Available from:  
1084 [https://rupress.org/jcb/article/146/3/659/43808/Myotactin-a-Novel-Hypodermal-](https://rupress.org/jcb/article/146/3/659/43808/Myotactin-a-Novel-Hypodermal-Protein-Involved-in)  
1085 [Protein-Involved-in](https://rupress.org/jcb/article/146/3/659/43808/Myotactin-a-Novel-Hypodermal-Protein-Involved-in)
- 1086 69. Gettner SN, Kenyon C, Reichardt LF. Characterization of beta pat-3 heterodimers, a  
1087 family of essential integrin receptors in *C. elegans*. *J Cell Biol*. 1995 May;129(4):1127–41.
- 1088 70. Williams BD, Waterston RH. Genes critical for muscle development and function in  
1089 *Caenorhabditis elegans* identified through lethal mutations. *J Cell Biol*. 1994  
1090 Feb;124(4):475–90.
- 1091 71. Gieseler K, Qadota H, Benian GM. Development, structure, and maintenance of *C.*  
1092 *elegans* body wall muscle. *WormBook*. 2017 Apr 13;2017:1–59.
- 1093 72. Boshier JM, Hahn BS, Legouis R, Sookhareea S, Weimer RM, Gansmuller A, et al. The  
1094 *Caenorhabditis elegans* *vab-10* spectraplakins isoforms protect the epidermis against  
1095 internal and external forces. *Journal of Cell Biology*. 2003 May 26;161(4):757–68.
- 1096 73. Karabinos A, Schmidt H, Harborth J, Schnabel R, Weber K. Essential roles for four  
1097 cytoplasmic intermediate filament proteins in *Caenorhabditis elegans* development. *Proc*  
1098 *Natl Acad Sci U S A* [Internet]. 2001 Jul 3;98(14):7863–8. Available from:  
1099 <http://www.ncbi.nlm.nih.gov/pubmed/11427699>
- 1100 74. Woo WM, Goncharov A, Jin Y, Chisholm AD. Intermediate filaments are required for *C.*  
1101 *elegans* epidermal elongation. *Dev Biol*. 2004 Mar 15;267(1):216–29.
- 1102 75. Karabinos A, Schulze E, Schünemann J, Parry DAD, Weber K. In vivo and in vitro evidence  
1103 that the four essential intermediate filament (IF) proteins A1, A2, A3 and B1 of the  
1104 nematode *Caenorhabditis elegans* form an obligate heteropolymeric IF system. *J Mol*  
1105 *Biol*. 2003 Oct 17;333(2):307–19.
- 1106 76. Hapiak V, Hresko MC, Schriefer LA, Saiyasisongkham K, Bercher M, Plenefisch J. *mua-6*, a  
1107 gene required for tissue integrity in *Caenorhabditis elegans*, encodes a cytoplasmic  
1108 intermediate filament. *Dev Biol*. 2003 Nov 15;263(2):330–42.

- 1109 77. Firestein BL, Rongo C. DLG-1 Is a MAGUK Similar to SAP97 and Is Required for Adherens  
1110 Junction Formation. *Mol Biol Cell*. 2001 Nov;12(11):3465–75.
- 1111 78. Peche V, Shekar S, Leichter M, Korte H, Schröder R, Schleicher M, et al. CAP2, cyclase-  
1112 associated protein 2, is a dual compartment protein. *Cellular and Molecular Life Sciences*.  
1113 2007 Oct;64(19–20):2702–15.
- 1114 79. Waddle JA, Cooper JA, Waterston RH. The alpha and beta subunits of nematode actin  
1115 capping protein function in yeast. *Mol Biol Cell [Internet]*. 1993 Sep;4(9):907–17.  
1116 Available from: <http://www.ncbi.nlm.nih.gov/pubmed/8257793>
- 1117 80. Edwards M, Zwolak A, Schafer DA, Sept D, Dominguez R, Cooper JA. Capping protein  
1118 regulators fine-tune actin assembly dynamics. Vol. 15, *Nature Reviews Molecular Cell*  
1119 *Biology*. Nature Publishing Group; 2014. p. 677–89.
- 1120 81. Klaavuniemi T, Yamashiro S, Ono S. *Caenorhabditis elegans* gelsolin-like protein 1 is a  
1121 novel actin filament-severing protein with four gelsolin-like repeats. *Journal of Biological*  
1122 *Chemistry*. 2008 Sep 19;283(38):26071–80.
- 1123 82. Ono S. Regulation of structure and function of sarcomeric actin filaments in striated  
1124 muscle of the nematode *Caenorhabditis elegans*. *Anat Rec (Hoboken) [Internet]*. 2014  
1125 Sep;297(9):1548–59. Available from: <http://www.ncbi.nlm.nih.gov/pubmed/25125169>
- 1126 83. Ray S, Agarwal P, Nitzan A, Nédélec F, Zaidel-Bar R. Actin-capping protein regulates  
1127 actomyosin contractility to maintain germline architecture in *C. elegans*. *Development*  
1128 (Cambridge). 2023 Mar 1;150(6).
- 1129 84. Ma L, Rohatgi R, Kirschner MW. The Arp2/3 complex mediates actin polymerization  
1130 induced by the small GTP-binding protein Cdc42. *Proceedings of the National Academy of*  
1131 *Sciences*. 1998 Dec 22;95(26):15362–7.
- 1132 85. Matas OB, Martínez-Menárguez JA, Egea G. Association of Cdc42/N-WASP/Arp2/3  
1133 signaling pathway with Golgi membranes. *Traffic*. 2004 Nov;5(11):838–46.
- 1134 86. Rohatgi R, Ma L, Miki H, Lopez M, Kirchhausen T, Takenawa T, et al. The Interaction  
1135 between N-WASP and the Arp2/3 Complex Links Cdc42-Dependent Signals to Actin  
1136 Assembly. *Cell*. 1999 Apr;97(2):221–31.
- 1137 87. Bu W, Lim KB, Yu YH, Chou AM, Sudhakaran T, Ahmed S. Cdc42 Interaction with N-WASP  
1138 and Toca-1 Regulates Membrane Tubulation, Vesicle Formation and Vesicle Motility:  
1139 Implications for Endocytosis. *PLoS One*. 2010 Aug 13;5(8):e12153.
- 1140 88. Ho HYH, Rohatgi R, Lebensohn AM, Le Ma, Li J, Gygi SP, et al. Toca-1 mediates Cdc42-  
1141 dependent actin nucleation by activating the N-WASP-WIP complex. *Cell*. 2004 Jul  
1142 23;118(2):203–16.
- 1143 89. Ferguson SM, De Camilli P. Dynamin, a membrane-remodelling GTPase. *Nat Rev Mol Cell*  
1144 *Biol*. 2012 Jan 11;13(2):75–88.
- 1145 90. Phillips CM, Updike DL. Germ granules and gene regulation in the *Caenorhabditis elegans*  
1146 germline. *Genetics*. 2022 Mar 3;220(3).
- 1147 91. Schisa JA, Pitt JN, Priess JR. Analysis of RNA associated with P granules in germ cells of *C.*  
1148 *elegans* adults. *Development*. 2001 Apr;128(8):1287–98.
- 1149 92. Brangwynne CP, Eckmann CR, Courson DS, Rybarska A, Hoegge C, Gharakhani J, et al.  
1150 Germline P granules are liquid droplets that localize by controlled  
1151 dissolution/condensation. *Science*. 2009 Jun 26;324(5935):1729–32.

- 1152 93. Seydoux G. The P Granules of *C. elegans*: A Genetic Model for the Study of RNA-Protein  
1153 Condensates. *J Mol Biol.* 2018 Nov 2;430(23):4702–10.
- 1154 94. Sheth U, Pitt J, Dennis S, Priess JR. Perinuclear P granules are the principal sites of mRNA  
1155 export in adult *C. elegans* germ cells. *Development.* 2010 Apr;137(8):1305–14.
- 1156 95. Chang HH, Miaw SC, Tseng W, Sun YW, Liu CC, Tsao HW, et al. PTPN22 Modulates  
1157 Macrophage Polarization and Susceptibility to Dextran Sulfate Sodium–Induced Colitis.  
1158 *The Journal of Immunology.* 2013 Sep 1;191(5):2134–43.
- 1159 96. Ghanta KS, Ishidate T, Mello CC. Microinjection for precision genome editing in  
1160 *Caenorhabditis elegans*. *STAR Protoc.* 2021 Sep 17;2(3).
- 1161 97. Davis MW, Jorgensen EM. ApE, A Plasmid Editor: A Freely Available DNA Manipulation  
1162 and Visualization Program. *Frontiers in Bioinformatics.* 2022;2.
- 1163 98. Montague TG, Cruz JM, Gagnon JA, Church GM, Valen E. CHOPCHOP: A CRISPR/Cas9 and  
1164 TALEN web tool for genome editing. *Nucleic Acids Res.* 2014 Jul 1;42(W1).
- 1165 99. Fay SF, Fay DS, Chhatre VE. CRISPRcruncher: A tool for engineering restriction sites into  
1166 coding regions. *MicroPubl Biol [Internet].* 2021 Jan 18;2021. Available from:  
1167 <http://www.ncbi.nlm.nih.gov/pubmed/33490886>
- 1168 100. Labun K, Montague TG, Gagnon JA, Thyme SB, Valen E. CHOPCHOP v2: a web tool for the  
1169 next generation of CRISPR genome engineering. *Nucleic Acids Res.* 2016 Jul  
1170 8;44(W1):W272–6.
- 1171 101. Labun K, Montague TG, Krause M, Torres Cleuren YN, Tjeldnes H, Valen E. CHOPCHOP v3:  
1172 Expanding the CRISPR web toolbox beyond genome editing. *Nucleic Acids Res.* 2019 Jul  
1173 1;47(W1):W171–4.
- 1174 102. Fire A, Xu S, Montgomery MK, Kostas SA, Driver SE, Mello CC. Potent and specific genetic  
1175 interference by double-stranded RNA in *Caenorhabditis elegans*. *Nature.* 1998 Feb  
1176 19;391(6669):806–11.
- 1177 103. Conte D, MacNei LT, Walhout AJM, Mello CC. RNA Interference in *Caenorhabditis*  
1178 *elegans*. *Curr Protoc Mol Biol.* 2015;2015:26.3.1-26.3.30.
- 1179 104. Kamath RS, Fraser AG, Dong Y, Poulin G, Durbin R, Gotta M, et al. Systematic functional  
1180 analysis of the *Caenorhabditis elegans* genome using RNAi. *Nature [Internet].* 2003 Jan  
1181 16;421(6920):231–7. Available from: <http://www.ncbi.nlm.nih.gov/pubmed/12529635>
- 1182 105. Sanchez AD, Feldman JL. A proximity labeling protocol to probe proximity interactions in  
1183 *C. elegans*. *STAR Protoc.* 2021 Dec 17;2(4).
- 1184 106. Wiśniewski JR, Zougman A, Nagaraj N, Mann M. Universal sample preparation method  
1185 for proteome analysis. *Nat Methods.* 2009 May;6(5):359–62.
- 1186 107. Searle BC, Pino LK, Egertson JD, Ting YS, Lawrence RT, MacLean BX, et al. Chromatogram  
1187 libraries improve peptide detection and quantification by data independent acquisition  
1188 mass spectrometry. *Nat Commun.* 2018 Dec 1;9(1).
- 1189 108. Graw S, Tang J, Zafar MK, Byrd AK, Bolden C, Peterson EC, et al. proteiNorm - A User-  
1190 Friendly Tool for Normalization and Analysis of TMT and Label-Free Protein  
1191 Quantification. *ACS Omega.* 2020 Oct 13;5(40):25625–33.
- 1192 109. Huber W, von Heydebreck A, Sültmann H, Poustka A, Vingron M. Variance stabilization  
1193 applied to microarray data calibration and to the quantification of differential expression.  
1194 *Bioinformatics.* 2002;18 Suppl 1:S96-104.

- 1195 110. Ritchie ME, Phipson B, Wu D, Hu Y, Law CW, Shi W, et al. Limma powers differential  
1196 expression analyses for RNA-sequencing and microarray studies. *Nucleic Acids Res.* 2015  
1197 Jan 6;43(7):e47.
- 1198 111. Thurman TJ, Washam CL, Alkam D, Bird JT, Gies A, Dhusia K, et al. proteoDA: a package  
1199 for quantitative proteomics. *J Open Source Softw [Internet]*. 2023 May 30;8(85):5184.  
1200 Available from: <https://joss.theoj.org/papers/10.21105/joss.05184>
- 1201 112. Alhamdoosh M, Ng M, Wilson NJ, Sheridan JM, Huynh H, Wilson MJ, et al. Combining  
1202 multiple tools outperforms individual methods in gene set enrichment analyses.  
1203 *Bioinformatics.* 2017 Feb 1;33(3):414–24.
- 1204 113. Fay DS, Gerow K. A biologist’s guide to statistical thinking and analysis. *WormBook.* 2013  
1205 Jul 9;1–54.
- 1206 114. Ge SX, Jung D, Yao R. ShinyGO: a graphical gene-set enrichment tool for animals and  
1207 plants. *Bioinformatics.* 2020 Apr 15;36(8):2628–9.
- 1208

1209

1210

1211

1212

1213

1214

1215

1216

1217

1218

1219

